The Astrophysical Journal, 893:118 (17pp), 2020 April 20 https://doi.org/10.3847/1538-4357/ab8003

The Impact of Realistic Foreground and Instrument Models on 21 cm Epoch of Reionization Experiments

A. Nasirudin[1,2], S. G. Murray[1,2,3], C. M. Trott[1,2], B. Greig[2,4], R. C. Joseph[1,2], and C. Power[2,5]
[1] International Centre for Radio Astronomy Research—Curtin University, Bentley, WA 6102, Australia; bella.nasirudin@icrar.org
[2] ARC Centre of Excellence for All Sky Astrophysics in 3 Dimensions (ASTRO 3D), Australia
[3] Arizona State University, Tempe, AZ, USA
[4] School of Physics—The University of Melbourne, VIC 3010, Australia
[5] International Centre for Radio Astronomy Research—The University of Western Australia, Crawley, WA 6009, Australia
Received 2019 December 3; revised 2020 March 10; accepted 2020 March 12; published 2020 April 22

Abstract

Predictions for the ability of 21 cm interferometric experiments to discriminate Epoch of Reionization (EoR) signal models are typically limited by the simplicity of data models, whereby foreground signals and characteristics of the instrument are often simplified or neglected. To move toward more realistic scenarios, we explore the effects of applying more realistic foreground and instrument models to the 21 cm signal, as well as the ability to estimate astrophysical parameters with these additional complexities. We use a highly optimized version of 21CMFAST, integrated into 21CMMC, to generate lightcones of the brightness temperature fluctuation for Bayesian parameter estimation. We include a statistical point-source foreground model and an instrument model based on the Murchison Widefield Array scaled in observation time to have an effective sensitivity similar to the future Square Kilometre Array. We also extend the current likelihood prescription to account for the presence of beam convolution and foregrounds, the two-dimensional power spectrum (PS), and the correlation of PS modes. We use frequency bands between 150 and 180 MHz to constrain the ionizing efficiency (ζ), the minimum virial temperature of halos ($T_{\rm vir}$), the soft X-ray emissivity per unit star formation rate (SFR) ($L_X/{\rm SFR}$), and the X-ray energy threshold (E_0). We find that the inclusion of realistic foregrounds and instrumental components biases the parameter constraints, due to unaccounted for cross-power between the EoR signal, foregrounds, and thermal noise. This causes estimates of ζ to be biased by up to 5σ, but the estimates of $T_{\rm vir}$, $L_X/{\rm SFR}$ and E_0 remain unaffected and are all within 1σ.

Unified Astronomy Thesaurus concepts: Reionization (1383); Cosmology (343); Large-scale structure of the universe (902); Astronomical instrumentation (799)

1. Introduction

The Cosmic Dawn (CD) and the subsequent Epoch of Reionization (EoR) mark the end of the cosmic dark ages, during which time the baryonic content of the dark, early universe existed in a warm, neutral state. The intergalactic medium (IGM), predominantly comprised of hydrogen, was illuminated by photons from the first ionizing sources, forming regions of reionized hydrogen with temperatures contrasting with the neutral IGM and background CMB (Barkana & Loeb 2001; Furlanetto et al. 2006). The significance of these periods is prevalent in almost all areas of astrophysics, particularly in understanding the transition between the current and early universe as well as the formation of primordial structures in the universe.

A key probe into these epochs is the imprint of the 21 cm spin-flip transition of neutral hydrogen (H I) that is redshifted into the low-frequency radio regime. Recently, the Experiment to Detect the Global Epoch of Reionization Signature published a measurement of a flattened absorption profile with timing that somewhat coincides with the expected H I signal from the CD (Bowman et al. 2018), although it needs further verification from independent experiments. Detection of the EoR, however, has not been reported and remains one of the key science goals of most current low-frequency interferometric telescopes, e.g., the Murchison Widefield Array (MWA; Tingay et al. 2013; Wayth et al. 2018), the Hydrogen Epoch of Reionization Experiment (HERA; DeBoer et al. 2017), and the Low Frequency Array (Van Haarlem et al. 2013).

Because direct imaging of the EoR remains beyond the sensitivity capabilities of current experiments, these instruments aim to detect the spatial fluctuations of the averaged power spectrum (PS). In the near future, however, upcoming low-frequency interferometers such as the Square Kilometre Array (SKA; Dewdney et al. 2009) and the final phase of HERA are expected to have the sensitivity to directly detect the tomographic imprints of the EoR.

Even with experiments focused on the detection of the variance instead of direct imaging of the EoR signal, its detection is still challenging due to astrophysical foregrounds and other contaminants. These include foregrounds from Galactic and extragalactic origins (Gleser et al. 2008; Jelić et al. 2010), ionospheric distortion (Jordan et al. 2017), instrument noise and radio frequency interference (Offringa et al. 2015). The foregrounds prove to be the primary contaminant, as they are expected to be up to five orders of magnitude brighter than the 21 cm signal (Pritchard & Loeb 2012). Various foreground mitigation and removal methods have been extensively studied; see, e.g., Liu & Shaw (2019) for details. However, for foreground removal methods such as source peeling, residual power is still left in the power spectrum, due to our incomplete knowledge of the extragalactic foregrounds. This is due to imperfect peeling and fainter sources existing below the peeling threshold (Datta et al. 2010; Morales et al. 2012; Trott et al. 2012; Vedantham et al. 2012).[6]

[6] In this work, we assume that the former is negligible and focus on the latter.

Exploration of a physical understanding of the EoR is performed through theoretical simulations of the sources and signal, to help supplement observations and constrain the signal. In particular, most simulation work has focused on establishing the roles of the first ionizing sources and finding the impact of astrophysical parameters on the H I signal (see, e.g., Barkana & Loeb 2001; Madau et al. 2004; Ricotti & Ostriker 2004; Knevitt et al. 2014). Although countless parameters may affect the EoR signal, whose estimates vary across the literature, some of the most influential EoR parameters (and their generally accepted estimates) include: the number of ionizing photons per baryon ($N_\gamma \sim 4000$) (Barkana & Loeb 2005); the power-law scale of the baryonic gas fraction in stars with source halo mass ($\alpha_* \approx 0.5$) (Behroozi & Silk 2015; Ocvirk et al. 2016); and the number of times a hydrogen atom recombines ($n_{\rm rec} \approx 1$) (Sobacchi & Mesinger 2014).

The ultimate goal of understanding the EoR from 21 cm observations will require constraining these parameters using theoretical models. It involves quantitatively evaluating the cosmic EoR signal by making use of one of the many existing EoR simulations, usually seminumerical, to extract information on the astrophysics. Aside from comparing the results of fiducial reionization simulations with experimental data (Choudhury & Ferrara 2005), other methods used to achieve this goal include using the maximum likelihood (χ^2) fitting (Barkana 2009), as well as Bayesian analyses via model selection (Binnie & Pritchard 2019) or Monte Carlo Markov Chain (MCMC) methods (see, e.g., Harker et al. 2011; Patil et al. 2014; Greig & Mesinger 2015; Hassan et al. 2017).[7] Alternative methods to on-the-fly MCMC sampling include emulating simulations using the power spectrum (Kern et al. 2017) and using artificial neural networks (Shimabukuro et al. 2017; Schmit & Pritchard 2017) or convolutional neural networks (Gillet et al. 2019).

A particularly powerful existing code that uses the MCMC approach is 21CMMC (Greig & Mesinger 2015, 2017, 2018), a parallelized, efficient EoR analysis code that wraps the publicly available EoR seminumerical simulator 21CMFAST (Mesinger et al. 2011) into its Bayesian MCMC framework to produce an EoR lightcone per iteration.[8] It uses the differential brightness temperature field, constructed as a lightcone, to compute the spherically averaged power spectrum that is, in turn, used in the likelihood prescription.

Previous applications of 21CMMC have used 21CMSENSE[9] to gauge the uncertainties in the one-dimensional (1D) power spectrum arising from the instrumental noise and smooth foregrounds, completely excising spherical k-modes dominated by the latter (Pober et al. 2013, 2014). While this approach is a good first-order approximation, it does not account for potential residual foreground contamination in k-modes that it uses due to more complicated instrumental systematics. This can cause difficulties in disentangling contamination and signal power, thus possibly leading to a biased estimate of reionization parameters. Moreover, it does not account for the induced chromaticity from the instrument on the 21 cm signal.

This work provides an extension to 21CMMC, in the publicly available plug-in PY21CMMC-FG. Using this framework, we aim to explore the impact of foreground and instrumental components on the ability to constrain the astrophysical parameters of the EoR. We apply a statistical point-source foreground model and an MWA-based instrument model to the 21CMMC lightcone outputs before averaging to a power spectrum. It is these "corrupted" lightcones that we use to estimate observed power spectra within the MCMC framework, thereby investigating more realistic constraints on astrophysical parameters.

The paper is structured as follows. We first set up the mathematical framework, which includes describing the foreground and instrumental effects we employ in our analysis, in Section 2. In Section 3, we analyze the observational effects on the EoR lightcones, and in Section 4, we present the MCMC analysis using 21CMMC with our pipeline. We then discuss the results in Section 5, and conclude in Section 6.

2. Mathematical Framework

2.1. Interferometric Visibilities

The baseline displacement, $\boldsymbol{u}$, is defined as $\boldsymbol{u} = \boldsymbol{x}/\lambda$, where $\boldsymbol{x}$ is the physical displacement between the baseline tiles and λ is the wavelength. We define the sky coordinate as $\boldsymbol{l} = (l, m) = (\sin\theta\cos\phi, \sin\theta\sin\phi)$, where θ is the zenith angle, and ϕ the angle around the zenith pole.

Based on these definitions, the measured correlation of the electric fields between two sensors for an interferometric observation, the visibility $V(\boldsymbol{u}, \nu)$ at frequency ν, in the flat-sky approximation is defined as

$$V(\boldsymbol{u}, \nu) = \int I(l, \nu) B(l, \nu) \exp(-2\pi i \boldsymbol{u} \cdot l) dl \quad [\mathrm{Jy}], \qquad (1)$$

with $I(l, \nu)$ and $B(l, \nu)$ being the intensity of each point source and beam attenuation at sky coordinate $\boldsymbol{l}$ and frequency ν, respectively. Using the flat-sky approximation whereby the effects of curvature are neglected, we assume that the observed interferometric visibility is identical to the Fourier transform of the product of signal and the beam model. We will address the second-order effects of spatial curvature on the visibility in future work.

2.2. Brightness Temperature and Power Spectrum

The EoR differential brightness temperature, δT_b, can be quantified by (Furlanetto et al. 2006)

$$\delta T_b(z) \approx 27 x_{\rm H\,I}(1 + \delta_{\rm nl}) \left(\frac{H(z)}{{\rm d}v/{\rm d}r + H(z)}\right)\left(1 - \frac{T_\gamma}{T_s}\right) \times \left(\frac{1+z}{10}\frac{0.15}{\Omega_m h^2}\right)^{\frac{1}{2}} \left(\frac{\Omega_b h^2}{0.023}\right) [\mathrm{mK}]. \qquad (2)$$

Here, $x_{\rm H\,I}$ is the neutral fraction, $\delta_{\rm nl}$ is the evolved Eulerian overdensity, H is the evolving Hubble constant, dv/dr is the gradient of the line-of-sight velocity component, T_γ is the temperature of the CMB, T_s is the spin temperature of H I, z is the redshift, Ω_m is the dimensionless matter density parameter,

[7] The recent work of Sims & Pober (2019) also uses an MCMC framework, but focuses on estimating the power spectrum band powers rather than astrophysical parameters, though it mentions a simple extension to do so.

[8] In this work, we use the most recent version available at https://github.com/BradGreig/Hybrid21cm. As of this writing, the most up-to-date version of 21CMMC has moved permanently to https://github.com/21cmFAST/21cmMC, and the underlying optimized 21CMFAST code has been modularized and exists at https://github.com/21cmFAST/21cmFAST.

[9] https://github.com/jpober/21cmSense

Ω_b is the dimensionless baryonic density parameter, and h is the normalized Hubble constant.

For interferometric observations, the PS is the primary metric used to characterize the EoR signal. It measures the spatial variance of a signal over a spatial volume V, and is defined as

$$P(k) \equiv \frac{|\langle \delta T_b^{\dagger}(\boldsymbol{k}) \delta T_b(\boldsymbol{k}) \rangle_{|\boldsymbol{k}|=k}|}{V} \quad [\mathrm{mK^2 Mpc^{-3} h^3}], \tag{3}$$

where k is the spatial scale in Fourier space. The PS can be computed either directly from the image cube or from the observed interferometric visibilities, whereby the signal is spherically averaged over the 3D spatial scales and is normalized by the volume of the observed area of the sky. The dimensionless 1D PS is given by

$$\Delta^2(k) = \frac{k^3}{2\pi^2} P(k) \quad [\mathrm{mK^2}], \tag{4}$$

and is routinely used in current experiments.

It is useful, however, to first compute the cylindrically averaged 2D PS, $P(k_\perp, k_\parallel)$. The angular and line-of-sight modes of the 2D PS, $k_\perp$ and $k_\parallel$, are converted from the Fourier dimensions following (Morales & Wyithe 2010)

$$k_\perp = \frac{2\pi |\boldsymbol{u}|}{D_M(z)} \quad [\mathrm{Mpc^{-1} h}], \tag{5}$$

and

$$k_\parallel = \frac{2\pi H_0 f_{21} E(z)}{c(1+z)^2} \eta \quad [\mathrm{Mpc^{-1} h}]. \tag{6}$$

Here, z is the observation redshift, $D_M(z)$ is the transverse comoving distance, H_0 is the Hubble constant, f_{21} is the rest frequency of the 21 cm hydrogen hyperfine transition, and $E(z)$ is defined as

$$E(z) = \sqrt{\Omega_m (1+z)^3 + \Omega_k (1+z)^2 + \Omega_\Lambda}, \tag{7}$$

where Ω_Λ and Ω_k are the dimensionless density parameters for dark energy and the curvature of space (Hogg 1999). Because the 2D PS bins the signal into separable perpendicular and line-of-sight modes, it effectively allows for the management of systematic effects arising from the different modes, and hence is commonly used as an initial step to decontaminate the cosmological EoR signal from the foregrounds. Colloquially termed the "wedge," the broad region of cylindrical k-space dominated by the foregrounds can be understood as the signature of smooth-spectrum foregrounds when being sampled by an imperfect instrument (Datta et al. 2010; Parsons et al. 2012; Trott et al. 2012; Vedantham et al. 2012). The key imperfections are the band-limiting attenuation due to the primary beam, and the discrete sampling of an interferometer, where the sampled wavemodes change with frequency ("chromaticity").

2.3. Components of Observable Signal

In this subsection, we present the mathematical framework of the different components of the observable signal, which is made of the EoR signal and foregrounds as observed by our instrument model.

Table 1
Fiducial Astrophysical Parameters and their Ranges Adopted in this Work

Parameter	Fiducial Value	Range
ζ	20.0	[10, 250]
$\log_{10}(T_{\mathrm{vir}})$	4.48	[4, 6]
$\log_{10}(L_X/\ \mathrm{SFR})$	40.5	[38, 42]
E_0	0.5	[0.1, 1.5]

2.3.1. EoR Lightcones and Parameters

We use a model δT_b field generated by 21CMFAST wrapped in 21CMMC. 21CMFAST is a seminumerical EoR modeling tool designed to efficiently simulate the 21 cm H I signal using approximate methods combining the excursion-set formalism (Bond et al. 1991; Furlanetto et al. 2004) and perturbation theory. The code generates realizations of δ_{nl}, ionization, peculiar velocity, and T_s in 3D, which are then combined to compute δT_b during the EoR. The astrophysical parameters involved in the code are customizable, allowing for the exploration of models and parameter space affecting the EoR (Mesinger et al. 2011, 2014).

The key parameters that we are primarily interested in are

1. the ionizing efficiency, i.e., the number of ionizing photons escaping into the IGM per baryon (ζ [dimensionless]);
2. the minimum virial temperature of halos required to form stars in galaxies (T_{vir} [K]);
3. the soft X-ray emissivity per unit star formation rate (SFR) escaping galaxies (L_X/SFR [erg s^{-1} keV^{-1} $M_\odot^{-1}$ yr]); and
4. the X-ray energy threshold for self-absorption by galaxies (E_0 [keV]).

These four parameters are chosen due to their relatively high influence on the δT_b field, as they directly affect the parameters governing T_b given by Equation (2), particularly $x_{\mathrm{H\,I}}$.[10] The fiducial values (and ranges) we adopt are based on Greig & Mesinger (2017), Park et al. (2019), and Gillet et al. (2019), and are summarized in Table 1. We note that we only use these values in our final analysis in Section 5. For exploration and validation purposes presented in Sections 3 and 4, we use the default parameters of $\zeta = 30$ and $\log_{10}(T_{\mathrm{vir}}/\mathrm{K}) = 4.7$. We also use the same random seed to generate the signal throughout this research.

We assume a Λ Cold Dark Matter universe using the default cosmological parameters values of 21CMFAST ($h = 0.68$, $\Omega_b = 0.048$, $\Omega_m = 0.31$, $\Omega_k = 0$, and $\Omega_\Lambda = 0.69$), consistent with results from Planck (2016).

The conversion from T_b to flux density $S(\nu)$ is given by the beam-modified Rayleigh–Jeans law,

$$S(\nu) = \left(\frac{2k_{\mathrm{B}} T_b}{A_{\mathrm{eff}}}\right) \Omega \times 10^{26} \quad [\mathrm{Jy}], \tag{8}$$

[10] 21CMMC now includes an updated parameterization that uses >6 parameters, but we chose this "legacy" set for ease of comparison to previous work.

where k_B is the Boltzmann constant, $A_{\rm eff}$ is the effective area of the tile (units of m^2), and Ω is the angular size of the beam (units sr).

2.3.2. Point-source Foreground Model

We use a simple point-source foreground model to simulate the effects of extragalactic foreground sources based on the power-law relation,

$$\frac{dN}{dS}(S, \nu) = \alpha S_\nu^{-\beta}\left(\frac{\nu}{\nu_0}\right)^{-\gamma\beta} [\mathrm{Jy}^{-1}\mathrm{sr}^{-1}]. \quad (9)$$

Here, dN/dS is the source spatial density per unit flux density, S_ν is the flux at a specific frequency ν, β is the slope of the source-count function, and γ is the mean spectral index of point sources. We fiducially use $\alpha = 4100$ Jy^{-1} sr^{-1}, $\beta = 1.59$, and $\gamma = 0.8$ at $\nu_0 = 150$ MHz based on an observational result from Intema et al. (2011).

Our adopted statistical foreground model, while an improvement over previous modeling in the context of parameter estimation, is by no means complete. It ignores potential point-source clustering (Murray et al. 2017), ionospheric effects (Mevius et al. 2016; Jordan et al. 2017; Trott et al. 2018), and more subtly, any potential correlations of the foregrounds with their antecedent EoR counterparts. More importantly, we have not included a galactic diffuse foreground model in this work. These effects are expected to be second-order, except for the diffuse emission, which is bright and spatially structured. These components are left as extensions to this work.

2.3.3. MWA and SKA-based Instrument Model

Our instrument components are based on the MWA (Tingay et al. 2013; Wayth et al. 2018) and the future SKA (Dewdney et al. 2009). The MWA is a low-frequency radio aperture array telescope located at the Murchison Radio Astronomy Observatory (MRO) site in Western Australia. The array consists of 128 connected tiles with an effective area per tile ($A_{\rm eff}$) of 21 m^2 at 150 MHz. Each tile consists of a 4×4 grid of dual polarization dipoles with a full width at half maximum field of view (FOV) of 26° at $\nu_0 = 150$ MHz. It operates in the 80–300 MHz frequency range, making it an excellent probe of the redshifted EoR signal. As one of its primary scientific goals, the MWA reionization observing scheme spans two 30 MHz bands, between 137 and 167 MHz and 167–197 MHz (Jacobs et al. 2016).

The low-frequency part of the future SKA (SKA-low) will be located at the MRO alongside the MWA (Dewdney et al. 2009; Mellema et al. 2013). It is expected to have a frequency resolution of 1 kHz with a frequency band of 50 to 200 MHz, and an FOV of 2.°5–10°.

The instruments themselves are hugely complicated: e.g., primary beam responses change between antennas, pointing, and polarization; the dipole array structure yields complex, frequency-dependent beam patterns; signal transport over coaxial cable can lead to cable reflections (imprinting frequency structure into the signal chain); and the large FOV introduces wide-field effects. We restrict ourselves to the primary instrumental response, including baseline sampling, FOV, and frequency-dependent primary beams, because these are the leading-order effects, and leave other instrumental effects to future work. We also neglect the fact that the Earth is rotating, and assume a fixed zenith pointing at the same patch of the sky. Neglecting the rotation of the Earth changes the UV coverage of the visibilities, hence the sample variance is different—and due to the wide FOV of the MWA, this amounts to a reduction of the overall thermal noise by (only) a factor of up to three on long baselines for the same total integration time. While this should be kept in mind, it is tangential to the point of our present work, and will be explored in more detail in future work.

We approximate the beam attenuation, $B(\boldsymbol{l}, \nu)$, to be Gaussian-shaped with

$$B(\boldsymbol{l}, \nu) = \exp\left(\frac{-|\boldsymbol{l}|^2}{\sigma^2_{\rm beam}(\nu)}\right), \quad (10)$$

where

$$\sigma_{\rm beam}(\nu) \simeq \frac{\epsilon\, c}{\nu D}. \quad (11)$$

Here, $\epsilon \simeq 0.42$ is the scaling from the more natural Airy disk to a Gaussian width, c is the speed of light, and D is the tile diameter (4 m for the MWA). Although the wide FOV of the MWA renders the flat-sky approximation (and hence Equation (1)) inaccurate (Thyagarajan et al. 2015a, 2015b), we will still use it as a reasonable first approximation, as the curved-sky treatment will be much more important when using a more realistic beam with side lobes, which enhances the "pitchfork" effect. We assume a fixed zenith pointing of the instrument over $\boldsymbol{l} \in (-1, 1)$, and pad the sky with zeros over three times the size of the sky in order to increase the resolution of the discrete Fourier transform.

We add thermal noise to our framework, corresponding to both measurement and radiometric noise. This is the uncertainty of the visibility arising from the finite number of samples, given by

$$\sigma_N = 10^{26}\frac{2k_B T_{\rm sys}}{A_{\rm eff}}\frac{1}{\sqrt{\Delta\nu\Delta t}} \quad [\mathrm{Jy}], \quad (12)$$

where $T_{\rm sys}$ is the system temperature, $\Delta\nu$ is the bandwidth of one frequency channel, and Δt is the integration time of the observation in seconds. In this equation, σ_N is essentially an estimation of the global sky signal (or temperature) for a given set of information that is dependent on the sky temperature, bandwidth, and sampling time for each visibility.

In addition, we use the un-normalized[11] Fourier Gaussian beam kernel in regridding the visibilities after baseline sampling, where the weight in cell i, w_i is given by

$$w_i = \exp(-[\pi\sigma_{\rm beam}(\nu)|\boldsymbol{u}_i - \boldsymbol{u}_j|]^2), \quad (13)$$

for baseline j. The gridded visibility $V_{\rm grid}(\boldsymbol{u}, \nu)$ is, hence, given by

$$V_{\rm grid}(\boldsymbol{u}, \nu) = \frac{\sum_{i=0}^{N_{\rm bl}} w_i V(\boldsymbol{u}_i, \nu)}{\sum_{i=0}^{N_{\rm bl}} w_i}, \quad (14)$$

where $N_{\rm bl}$ is the number of all included baselines. A Blackman–Harris frequency taper ($H(\nu)$) has also been applied to reduce spectral leakage in the side lobes due to the limited bandwidth. Note that we do not normalize the beam and taper,

[11] The normalization cancels out in Equation (14).

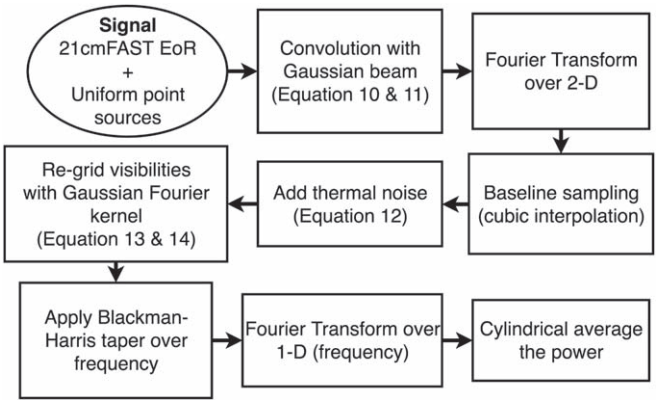

Figure 1. Summary of our instrumental algorithm.

but the steps we have taken are consistent with those taken by current 21 cm experiments.

2.3.4. The 2D Power Spectrum

In this work, we mostly use observational units, hence $k_\perp$ and $k_\parallel$ are known as u [unitless] and η [1/MHz], respectively, and the 2D PS ($P(\boldsymbol{u}, \eta)$) is in units of $\mathrm{Jy}^2\ \mathrm{Hz}^2$. We compute $P(\boldsymbol{u}, \eta)$ by cylindrically averaging the power of the visibilities within radial bin $\boldsymbol{u}$,

$$P(\boldsymbol{u}, \eta) \equiv \frac{\sum^{\boldsymbol{u}_i<\boldsymbol{u}} V^{\dagger}_{\mathrm{grid}}(\boldsymbol{u}_i, \eta) V_{\mathrm{grid}}(\boldsymbol{u}_i, \eta)}{\sum^{\boldsymbol{u}_i<\boldsymbol{u}} \left(\sum_{i=0}^{N_{\mathrm{bl}}} w_i\right)} \quad [\mathrm{Jy}^2\mathrm{Hz}^2], \tag{15}$$

where

$$V_{\mathrm{grid}}(\boldsymbol{u}, \eta) = \int V_{\mathrm{grid}}(\boldsymbol{u}, \nu) H(\nu) \exp(-2\pi i \eta \cdot \nu) d\nu \quad [\mathrm{JyHz}]. \tag{16}$$

The full algorithm from Sections 2.3.3 and 2.3.4 is summarized in Figure 1.

2.4. Bayesian Parameter Estimation

Bayesian parameter estimation through Monte Carlo Markov Chain (MCMC) is a powerful algorithm that is widely used in a variety of scientific fields to constrain parameters of interest by determining their full posterior distribution. We have chosen to use 21CMMC, an MCMC analysis tool designed to estimate astrophysical parameter constraints from the EoR. It incorporates EoR simulation data produced on the fly by an optimized version of 21CMFAST to statistically compare the models to either mock or observed data (Greig & Mesinger 2015).

The existing log-likelihood prescription used by 21CMMC uses the 1D PS and is given by:

$$\ln \mathcal{L} = -\frac{1}{2} \sum_j \frac{(P_D(k_j) - P_M(\theta, k_j)^2}{\sigma_D^2(k_j) + (\alpha P_M(\theta, k_j)^2}, \tag{17}$$

where P_D is the 1D PS of the experiment or mock data, P_M is the model 1D PS, θ is the set of EoR parameters for the model, and σ_D^2 is the uncertainty of the experiment computed using 21CMSENSE (Pober et al. 2014). In this equation, α is a variable corresponding to the uncertainty of the model, often set to 10–20% by inspecting how close 21CMFAST is to radiative transfer models, with 15% being the default value. All estimates are a function of wavenumber, k. In the presence of foregrounds and the instrumental beam, this prescription is only optimal[12] if the following set of conditions is satisfied:

1. The brightness temperature fluctuations are truly Gaussian.
2. The EoR signal is 3D isotropic.
3. The sources of uncertainty have 3D isotropic signal.
4. The PS modes for both the EoR and foregrounds are Gaussian.
5. The PS modes are independent for both the EoR and foregrounds.
6. The foreground noise is independent of the EoR parameters.

We postulate that the first and second conditions are valid first-order assumptions and we leave the last one for future work. We discuss and address the others, along with a summary of our improvements to 21CMMC, in the following subsections.

2.4.1. The 3D Isotropic Uncertainties

The 1D PS is employed because it provides complete information about the isotropic EoR signal. However, it confounds the impact of foregrounds because they naturally reside in a larger cylindrical Fourier space (i.e., smooth-spectrum versus angular clustering). In a 1D PS, the wedge-mode contaminates the entire annulus because the foregrounds show a nonisotropic signature, corrupting some otherwise good modes. Although some sort of avoidance method is typically used to minimize the corruption of 1D PS modes, it does not account for the full information.

We extend the likelihood formalism by using the 2D PS instead of the 1D PS, as it allows for the management of systematic effects arising from $k_\perp$ and $k_\parallel$ modes, respectively. The 2D PS is commonly used as an initial step to decontaminate the cosmological EoR signal from the foregrounds in the forms of the "wedge" and the "EoR window." Foreground power dominates the lower $k_\parallel$ modes, yielding higher variance in the wedge as compared to the EoR window. Using the 2D PS means that modes in the same $|\boldsymbol{k}|$-annulus that may come from different $k_\parallel$ modes (from within and without the wedge) can be treated independently, and therefore the full information can be extracted.

2.4.2. Gaussianity and Independence of Instrument-convolved Foregrounds

In Equation (17), the use of σ_D^2 follows the assumption that the input data are Gaussian and independent. While this will hold true for the EoR signal, because the cosmological signal is close to Gaussian, in the presence of foregrounds and instrumental effects, this assumption might break. We will focus on investigating the Gaussianity and independence of the instrument-convolved foregrounds, because the variance of the data is dominated by the variance of the foregrounds in most bins. This can then dictate the appropriate formalism to adopt, without adding unnecessary complexity. Because we have established in the previous subsection that we will be using the 2D PS to accommodate the presence of foregrounds, we will continue this discussion using the 2D PS of instrument-convolved foregrounds that were simulated based on our

[12] It uses all available information to generate the likelihood—and therefore posterior—rather than losing some information by improper assumptions

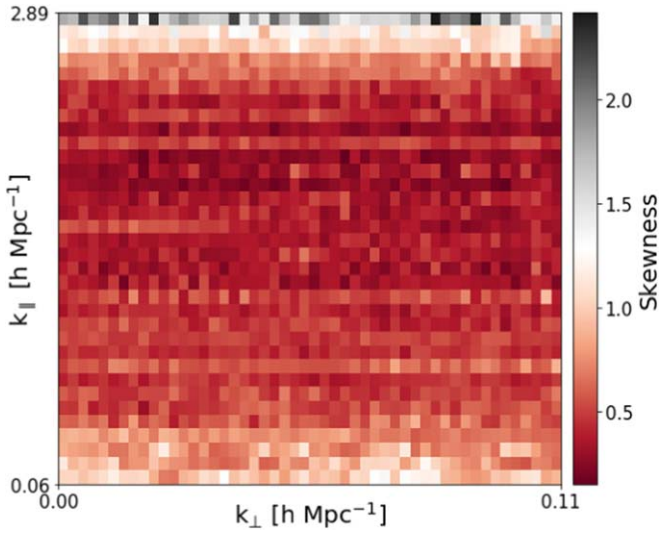

Figure 2. Skewness of the 2D PS of the instrument-convolved point-source foregrounds. Bins are predominantly close to Gaussian over the primary range of interest (0.1 to 1 h Mpc^{-1}).

models; the ensemble is then used to compute the skewness and correlation in each 2D mode.

We investigate the Gaussianity of the 2D PS by finding the skewness in bins of $k_\perp$ and $k_\parallel$. The skewness measures the asymmetry of the probability distribution about its mean, with a skewness of zero being perfectly symmetric and increasing skewness showing increasing asymmetry. Figure 2 shows the skewness of the 2D PS of the instrument-convolved point-source foregrounds. Over the primary range of interest (0.1 to 1 h Mpc^{-1}), the bins are predominantly close to Gaussian. Regions of higher skewness are found only at either high $k_\parallel$, where the signal is low, or at low $k_\parallel$, where the foregrounds are strong and the mode is therefore heavily downweighted in the likelihood—and thus in our fits for the underlying parameters θ. Ergo, we are content to maintain the assumption of a Gaussian likelihood.

We investigate the assumption of independence of the instrument-convolved foreground model by finding the correlation coefficient between $k_\perp$ and $k_\parallel$ bins in the 2D PS. The correlation measures the strength of the joint variability of two random variables, in this case the bins of $k_\perp$ and $k_\parallel$, with possible values ranging from -1 (completely anticorrelated) to $+1$ (completely correlated). As with Gaussianity (see Section 2.4.2), we focus on the foregrounds rather than the 21 cm signal.

Figure 3 shows the correlation coefficient of the 2D PS of the instrument-convolved foregrounds of four individual ($k_\perp$, $k_\parallel$) bins with all other bins. The right and bottom subpanels of each major panel show the correlation coefficient along a 1D slice (in the displayed dimension) through the selected 2D bin of each main panel. The dotted black line divides the area between the wedge and the EoR window. As expected, each chosen ($k_\perp$, $k_\parallel$) bin is completely correlated with itself (black cell in main panels corresponding to highest point in the smaller side panels). However, we can also see that the bin is highly correlated over $k_\parallel$ and the correlation spills over to the two $k_\perp$ bins adjacent to the chosen bin. This is due to the frequency-dependence of the instrument, resulting in chromatic mode mixing of foregrounds (Datta et al. 2010; Morales et al. 2012; Trott et al. 2012; Vedantham et al. 2012). As such, we can conclude that the 2D PS of the instrument-convolved foregrounds is not independent between modes and that we must use the covariance, instead of the variance, in the likelihood prescription. Neglecting the dependence of the modes may result in overconstraining of parameters, regardless of whether the PS is 1D or 2D.

We thus extend the likelihood prescription to use the multivariate normal likelihood, $\ln \mathcal{L}$, following the use of the 2D PS and the presence of foregrounds. Here, $\ln \mathcal{L}$ is given by

$$\ln \mathcal{L} = -\frac{1}{2}[(P_D - P_M(\boldsymbol{\theta})^T \Sigma^{-1}(P_D - P_M(\boldsymbol{\theta})], \tag{18}$$

where Σ is the covariance[13] of our *fiducial* noise and foreground ($N+\mathrm{FG}$) model with the addition of sample variance (second term of following equation), so that the total variance, σ_T^2, is given by

$$\sigma_T^2 = \sigma^2(P_{N+\mathrm{FG};M}) + \frac{P_{21;M}^2}{\sum_j \left(\sum_{i=0}^{N_{\mathrm{bl}}} w_i\right)^2}; \tag{19}$$

$$P_D = P_D(k_\perp, k_\parallel) = P_{21+N+\mathrm{FG};D} \tag{20}$$

is the (mock) data PS, assumed to be comprised of a 21 cm component and a noise and foreground component; and

$$P_M(k_\perp, k_\parallel|\boldsymbol{\theta}) = P_{21}(k_\perp, k_\parallel|\boldsymbol{\theta}_{21}) + P_{N+\mathrm{FG}}(k_\perp, k_\parallel|\boldsymbol{\theta}_{N+\mathrm{FG}}) \tag{21}$$

is a parameter-dependent *model* of the data. Note that we use the *expected* power of noise and foregrounds instead of just one specific realization for the model. Because it is computationally expensive and difficult to calculate the expected power of all components at each iteration, we have modeled the 21 cm signal separately and use the same expected foregrounds and noise power each time, which is possible because we do not have the $\theta_{N+\mathrm{FG}}$ parameter in the likelihood. This also assumes that the cross-power[14] terms are negligible and is a reasonable first-order approximation consistent with other works; however, we will see in Section 5 that this assumption is not true.

Note that P_D and P_M are *not* the true power spectrum computed from the simulation box. They are related to the true power spectrum, P^*, by $P = \hat{W}P^*$, where $\hat{W}$ is all the window functions that encompasses the instrumental and analysis effects (such as the beam and frequency taper) used in this research. The fact that we compute P_D, P_M, and Σ using exactly the same pipeline means that they are self-consistent, hence the effects of $\hat{W}$ should cancel out in the likelihood. Note also that the form of Equation (18) explicitly assumes that the covariance does not depend strongly on the astrophysical parameters. Otherwise, it would require an extra term of $-\ln\det(\Sigma^{-1})$. This is a reasonable assumption for most cylindrical k-modes, which are dominated by foregrounds whose parameters we are not directly interested in.

[13] Σ is computed numerically using the Monte Carlo method to simulate the noise and foreground over 1000 random realizations at the fiducial parameters. The ensemble of realizations is passed through the algorithm summarized in Figure 1 to produce the 2D PS and calculate Σ. This is precomputed prior to the MCMC. We note that the covariance may not have converged (see, e.g., Dodelson & Schneider 2013 and Taylor & Joachimi 2014), hence further investigation is necessary, but we have left this for future work.

[14] An explicit derivation of its variance is shown later in Section 5 (Equation (23)).

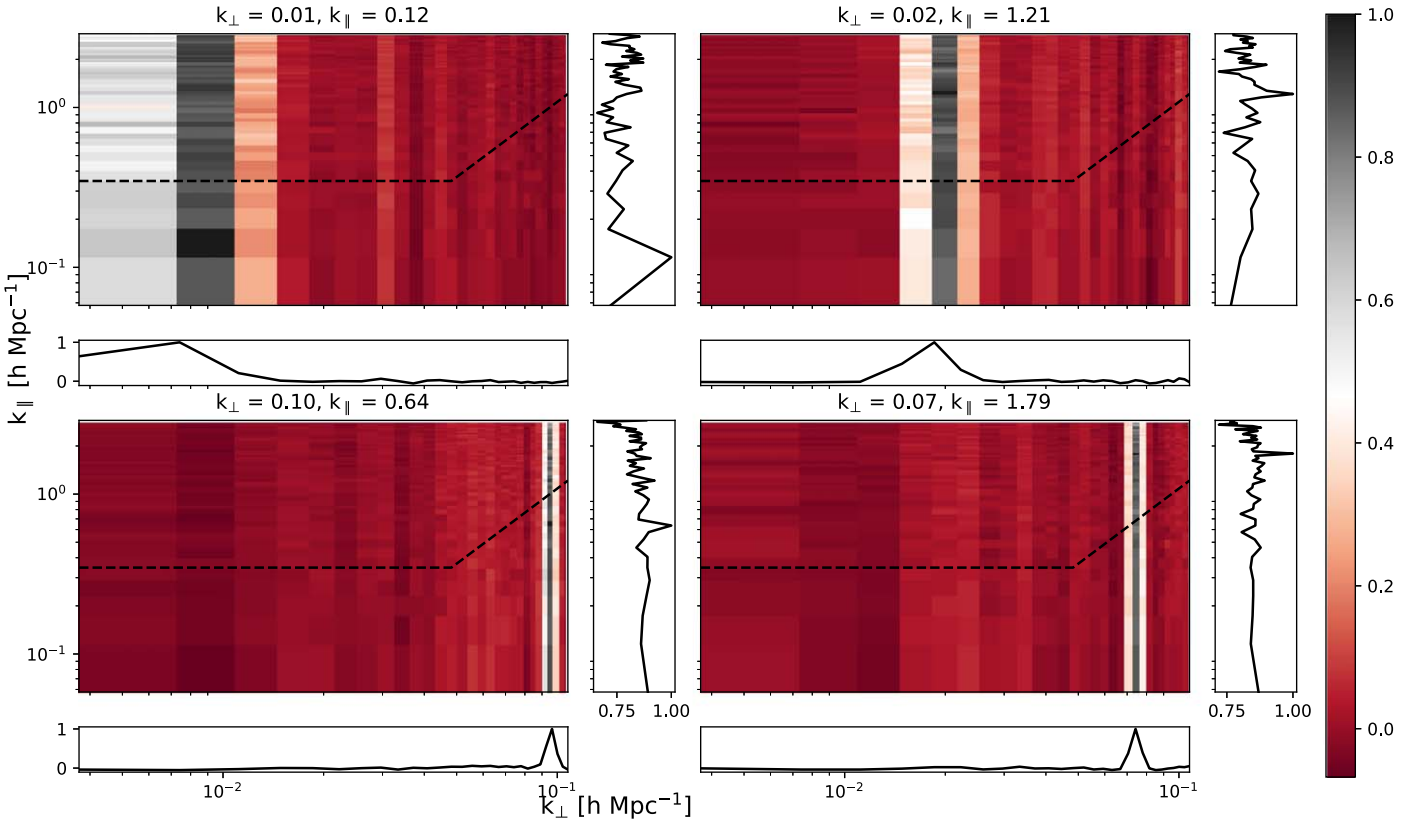

Figure 3. Correlation coefficient of the 2D PS of the instrument-convolved foregrounds between a single cell with all other cells. The horizontal and vertical plots show cuts through the 2D space at the chosen single-cell locations, demonstrating the degree of correlation in the angular and line-of-sight modes. Each chosen ($k_\perp$, $k_\parallel$) bin is completely correlated with itself (black cell in main panels corresponding to highest point in the smaller side panels). However, also note that the bin is highly correlated over $k_\parallel$ and the correlation spills over to the two $k_\perp$ bins adjacent to the chosen bin.

2.5. Extensions to 21CMMC

The foregrounds and instrumental components, along with other improvements developed in this work and described in the previous sections, are combined in a publicly available plug-in to the new 21CMMC, called PY21CMMC-FG.[15] It makes use of 21CMMC's new ability to allow the user to arbitrarily insert code to modify the lightcone before producing a likelihood. This creates realizations of the EoR signal obscured by the foregrounds, which are measured by an instrument model and then used as input to the log-likelihood.

To summarize, the extensions to 21CMMC that are available in PY21CMMC-FG include:

1. *A foreground model*: includes both diffuse and point-source foregrounds (although only the latter is used in this work for simplicity).
2. *An instrument model*: includes a Gaussian beam model, the array baseline sampling, and thermal noise.
3. *Calculation of the 2D PS*: to separate the cosmological EoR signal from the foregrounds.
4. *The covariance of the PS*: to account for the correlated instrument-convolved foregrounds.
5. *The likelihood prescriptions for the MCMC*: expand to multivariate normal distribution.
6. *Stitching of the lightcones*: to account for the wide FOV of the instrumental beam model.
7. *Padding of the sky*: to increase the image resolution for Fourier transform.
8. *Fourier beam gridding kernel*: to properly interpolate, average, and weight visibilities onto a grid.

All of these have been discussed in detail in this section, except for the stitching of the lightcones. We will discuss that in the next section (Section 3) when we explore the observational effects on the EoR lightcones.

2.6. Comparison to Existing Framework

The final focus of this section is to compare the uncertainty level from our framework, PY21CMMC-FG, to that from the publicly available existing framework, 21CMSENSE (Pober et al. 2013, 2014). In general, 21CMSENSE performs a separate calculation of the instrument sensitivity arising from thermal noise and cosmic variance while avoiding the foreground-dominated region; the uncertainty file is then used as input into 21CMMC. For more details, we refer readers to Pober et al. (2013) and Pober et al. (2014).

For 21CMSENSE, we adopt the drift scan mode and "moderate" foreground removal with the MWA Phase II baselines, $A_{\rm eff} = 21$ m^2 and $T_{\rm sys} = 240$ K. We also use $\Delta t = 2 \times 10^5$ hr in both frameworks. The reasoning behind this value is explained in detail in Section 4, but in general, we use this value so that we can approximate the noise level for 1000 hr observation of the future SKA_LOW1.

Note that the uncertainty with sample variance is calculated differently in the two frameworks. Our framework calculates

[15] Found at https://github.com/BellaNasirudin/py21cmmc_fg.

Table 2
The Differences between 21cmSense and py21cmmc-fg

	21cmSense	py21cmmc-fg
PS	1D	2D
Frequency-dependent baselines	No	Yes
Cross-power in variance	Yes	No
Foregrounds	Avoidance	Suppression
Earth rotation synthesis	Yes	No
Baseline sampling on EoR PS	No	Yes
Frequency taper	No	Yes
Gridding kernel	No	Yes

σ_T^2 based on Equation (19), while 21cmSense defines σ_T^2 as

$$\sigma_T^2(k) = \left(\sum_i \frac{1}{(P_{21}(k) + P_{N,i}(k)^2} \right)^{-\frac{1}{2}}, \quad (22)$$

whereby an inverse-weighted summation is performed over the UV cell i for each k mode bin (Pober et al. 2013). The main difference between the two frameworks is the presence of the cross-terms between the EoR PS and the noise variance for 21cmSense.

In addition to the calculation of sample variance, 21cmSense and py21cmmc-fg have a few key differences that can affect the total uncertainty level. We have summarized these differences in Table 2. The resulting total uncertainties from the two frameworks are presented in Figure 4. The total uncertainties loosely match at the relevant modes where the signal dominates, with a difference of less than half an order of magnitude. At high k, however, the difference is as high as one order of magnitude. We attribute the difference in total uncertainty to the missing Earth rotation synthesis, which essentially fills up more UV space and hence increases the overall noise level (i.e., fewer modes can combine coherently). Even though the Fourier beam gridding kernel we employ partly takes this into account, it does not restore the noise to the full level that it would be at with a proper rotation synthesis. We note that this is a shortcoming of our framework, and ameliorating it is left for future work.

3. Observational Effects on EoR Lightcones

In this section, we explore the observational effects of adding foregrounds to the EoR signal. This is first done by explaining the steps we have taken to ensure that both the EoR signal and foregrounds can be added together. We then analyze the effects on the 1D and 2D power spectra and compare the differences in image space.

In order for us to add the foreground and EoR lightcones, they need to cover the same angular size and have the same angular resolution. At $z = 6$, the resulting angular sky size of a 1 Gpc h^{-1} simulation box, which is considered to be large in theoretical studies, is merely $\sim$0.12 rad. On the other hand, the FOV of the MWA is $\sim$1 rad. Running a massive box that covers the MWA FOV is unrealistic and computationally expensive, so instead, we have made a realization of the lightcone across the mock sky by assuming that the same structure is periodically repeated. To preserve the wavenumber,

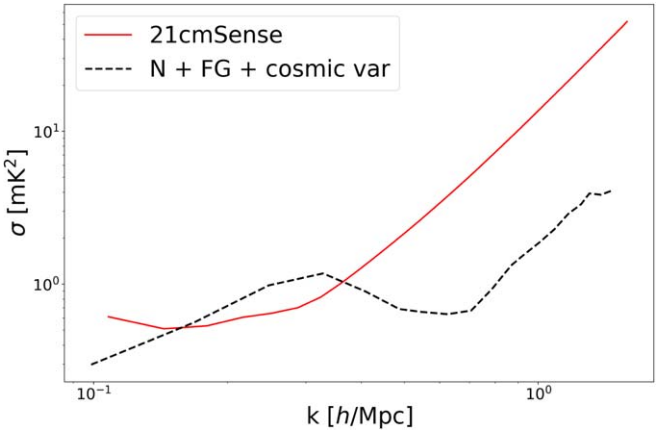

Figure 4. Total uncertainty from 21cmSense (red solid line) compared to the total uncertainty from our framework (black dash line) with $T_{\rm sys} = 240$ K and $\Delta t = 2 \times 10^5$ hr.

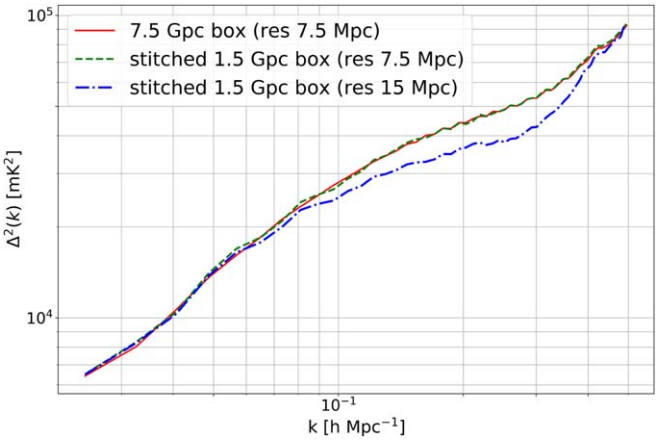

Figure 5. Comparison of the 1D PS of the 7.5 Gpc box (red), the stitched 1.5 Gpc box (green dotted), and the stitched 1.5 Gpc coarsened to a resolution of 15 Mpc (blue dashed–dotted). The 7.5 Gpc box and the stitched 1.5 Gpc box agree very well on most scales, but the 1D PS of the stitched and coarsened box differs from the 1.5 Gpc box at high k, due to finite resolution.

we have ensured that the full box is used in the stitching, i.e., we use an integer number of boxes. We also limit ourselves to using scales smaller than the box size in the parameter estimation to avoid systematics due to this repetition.

Furthermore, due to memory limitations, we have opted to coarsen the EoR signal using interpolation. Of course, the coarsening process can be avoided by setting the EoR lightcone from 21cmFAST to be of the same angular size. This, however, will affect the small-scale processes involved in determining δT_b, so we prefer to perform the coarsening post-stitching.

To study the effects of tiling and coarsening of the lightcone, we use simulation boxes of size 1.5 and 7.5 Gpc, both with a resolution of 7.5 Mpc. While we will typically work with the 2D PS, we use the 1D PS when comparing data quantitatively in this section. We compare the 1D PS of the 7.5 Gpc box, the stitched 1.5 Gpc box, and the stitched 1.5 Gpc coarsened to a resolution of 15 Mpc in Figure 5. The y-axis shows the dimensionless 1D PS, while the x-axis shows the k scales.

The 7.5 Gpc box and the stitched 1.5 Gpc box agree very well on most scales, suggesting that stitching the box does not negatively affect the PS. However, the 1D PS of the stitched

and coarsened box differs from the 1.5 Gpc box at high k.[16] This is, of course, expected because the coarsening of the box results in a different resolution, thus affecting the small scale structure of the δT_b. The stitching of boxes and coarsening of the resolution may potentially affect the statistics of the PS, due to lack of cosmic variance.

Herein, we have been presenting plots in cosmological units. In the code and hereafter in the paper, we have opted for observation units of Jy, Hz, and radians, to minimize inconsistencies and errors in converting between the two units. Note that the choice of units is inconsequential for the likelihood, as long as the same units are used in the numerator and the denominator.

4. MCMC Analysis

For parameter estimation, we use an EoR lightcone of size $750\,h^{-1}$Mpc with 250 cells. The lightcone is stitched together to cover 1 steradian of the sky and coarsened to 800 cells (resolution of $\approx 24\,h^{-1}$Mpc) before being padded by zeros to three times the sky size in order to increase the resolution for the Fourier transform. The bandwidth of the observation is 10 MHz, from 150 to 160 MHz, with 100 frequency channels. We assume that $T_{\rm sys} = 240$ K, corresponding to the average sky temperature at 150 MHz.

To ensure that our MCMC framework is consistent, we first perform simpler tests in which we attempt to loosely constrain only two parameters, ζ and $T_{\rm vir}$ (with fiducial values of $\zeta = 30.0$ and $T_{\rm vir} = 4.7\ \log_{10}$K). These systematic tests include

1. Uniform—regular and filled—UV sampling with no thermal noise or foregrounds;
2. Uniform UV sampling with point-source foregrounds but no thermal noise;
3. Uniform UV sampling with thermal noise but no foregrounds;
4. MWA baseline sampling with thermal noise but no foregrounds; and
5. MWA baseline sampling with thermal noise and point-source foregrounds.

Step 5 constitutes the end-goal of this work (but with all four parameters from Table 1). Note that, with these tests, we are not interested in properly estimating the values of the parameters; we only want to gauge whether the MCMC walkers would assemble around the right values, ergo the burn-in phases of the walkers are still included in this section. We initially set the observation time to 1000 hr, consistent with other research, but the observation time is later increased to 2×10^5 hr (the motivation of which is explained later in this section). To clarify, only steps 1–3 are done with 1000 hr of observation time. The final two steps, along with everything else after, are done with 2×10^5 hr.

We present a corner plot of our checks in Figure 6, which shows the projection of the values of the parameters over 1D and 2D space density. The black dashed lines show the actual value of the parameter, while the colored, shaded regions show the values of the estimated parameter that have been projected over the density space in 1D (diagonal plots) and 2D (nondiagonal plots).

[16] The curves converge again at high k because modes $\geqslant 0.2$ h/Mpc (corresponding to the Nyquist value) are not reliable.

It is clear that convolving the stitched and coarsened EoR signal with the Gaussian beam and implementing the 2D PS and the multivariate normal distribution in the likelihood prescription do not negatively impact the parameter estimation, as apparent from the constraints from Step 1 (blue region). The addition of point-source foregrounds in Step 2 (orange) does not significantly expand the constraints. This can be attributed to the fact that the foreground contamination is fully contained at smaller η, due to the uniform UV sampling.

However, with the addition of thermal noise in Step 3 (green region), the peak of the distribution is significantly shifted with respect to the true value, indicating that the results are biased. We note also that the artificial "uniform" UV sampling unnecessarily inflates the impact of thermal noise, as it restricts the number of baselines per UV cell to one. To investigate the cause of the bias, we plot the 2D PS of the EoR signal and the thermal noise, presented in Figure 7. With the uniform UV sampling, the signal-to-noise ratio is of order unity for 1000 hr of observation time, due to the small collecting area of the MWA, either with the MWA baselines sampling or the uniform UV sampling. While this is enough for an EoR signal detection over the slope of the 1D PS, it is not sensitive enough for EoR parameter estimation with the MWA.

To enable parameter constraints for the remainder of the work, we henceforth increase Δt in Equation (12) to 2×10^5 hr for the MWA-based instrument model that we have. This Δt is equivalent to adopting an SKA-like sensitivity for which $A_{\rm eff} = 300\,{\rm m}^2$, but is achievable with only 1000 hr. As seen in Step 4 (red region), both the use of the larger collecting area and the presence of UV sampling reduce the noise, resulting in the MCMC converging to the model values.

In Step 5 (purple region), the presence of point-source foregrounds expands the posteriors by 100% compared to thermal noise alone without bias. The reason the purple contour is larger than the red, while the orange is not larger than the blue, is that nonuniform sampling implies chromaticity, which creates the wedge and therefore removes many otherwise useful modes.

5. Parameter Estimation Results

Now that we have established the robustness of our additional model complexities, we can use the MWA baseline sampling with thermal noise and point-source foregrounds to constrain the four reionization parameters in Table 1. We use three different frequency bands: 150–160, 160–170, and 170–180 MHz, to observe the EoR signal, which is obscured by point-source foregrounds in the presence of instrumental effects and thermal noise.

Before we proceed with our results, we would like to emphasize that our pipeline is computationally intensive and time-consuming. With five chains run for each parameter, we have 20 walkers in total. One iteration per walker uses 10 GB of memory per node and takes roughly 20 minutes to completely simulate the EoR brightness temperature field, tile and coarsen it to cover the whole sky, add a Gaussian beam, Fourier transform the beam-convolved sky, sample the UV sample, and regrid the visibilities and cylindrically average them to find the 2D PS before finding the log-likelihood. The bottleneck of our pipeline is in regridding the visibilities using a Gaussian beam kernel after baseline sampling, which takes around 15 minutes to complete.

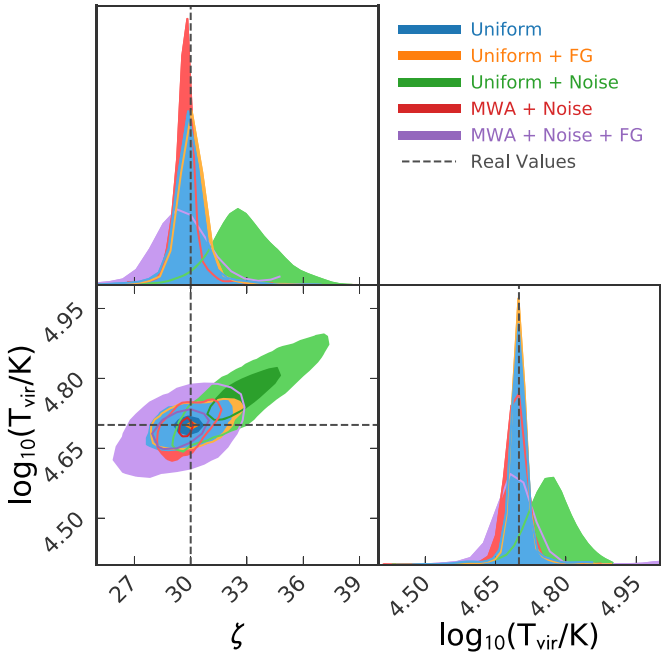

Figure 6. Corner plot comparing the constraints on our systematic tests: uniform UV sampling with no thermal noise or foregrounds (blue); uniform UV sampling with point-source foregrounds but no thermal noise (orange); uniform UV sampling with 1000 hr of thermal noise with the MWA but no foregrounds (green); MWA baseline sampling with 2×10^5 hr of thermal noise with the MWA but no foregrounds (red); MWA baseline sampling with 2×10^5 hr of thermal noise with the MWA and point-source foregrounds (purple). Using 2×10^5 hr of thermal noise with the MWA is comparable to the noise level of 1000 hr with the SKA. Artificial "uniform" UV sampling unnecessarily inflates the impact of thermal noise (green), as it restricts the number of baselines per UV cell to one and the small collecting area of the MWA gives a signal-to-noise ratio of order unity; both of these factors results in a biased estimate. With the addition of baselines sampling and the use of SKA sensitivity, the constraints remain unbiased (purple and red), although the final test (red) gives a very inflated constraint compared to the other tests. Note that these constraints still have the burn-in phase included.

To test the performance, we use a Gaussian process model to fit for the maximum likelihood autocorrelation function, which is used to estimate the autocorrelation time, τ. We found that $\tau \approx 200$ iterations, irrespective of which frequency band is being used, with the recommended total iteration being 50τ. However, because of the memory and time limitations we have mentioned above, we have only run our chains up to around 5τ. This is not enough to definitively claim that our chains have properly converged, but the results we currently have are useful to give an initial estimate of how well we can constrain the EoR parameters in the presence of foregrounds and thermal noise with our pipeline, as well as to gauge the plausibility of our assumptions.

Furthermore, in calculating our constraints, we have ignored walkers that are stuck in local minima. An example of this is shown in Figure 8, where we have plotted the trace plots that show the values of the four EoR parameters at every iteration and the corresponding $\ln \mathcal{L}$ after burn-in for the 160–170 MHz band with thermal noise and foregrounds. In this particular case, we have ignored the walkers with $\ln \mathcal{L} < -4000$.

We present a corner plot of the different observation bands in Figure 9, in which the orange, green, and blue shaded regions represent the 150–160, 160–170, and 170–180 MHz bands, respectively. The black dashed lines show the true values of the parameters ($\zeta = 20$, $\log_{10}(T_{\rm vir}) = 4.48$, $L_X/{\rm SFR} = 40.5$, and $E_0 = 0.5$ keV). The darker/lighter shaded regions represent $1\sigma/2\sigma$ confidence regions corresponding to the 84th and 16th percentiles. From the figure, it is clear that $L_X/{\rm SFR}$ and E_0 are relatively unconstrained in all frequency bands and that $T_{\rm vir}$ is tightly constrained. Note that ζ and $T_{\rm vir}$ are quite correlated and biased in all bands. This is especially true for the 160–170 MHz band, in which the green region is further from the truth values. The bias suggests that the primary effects of ζ and $T_{\rm vir}$ are on regions that are most affected by foregrounds on the larger scales. A bias indicates either a very anomalous noise realization (more than two sigma over the whole 2D parameter space) or an incorrect model.

To investigate the reason for the bias in the presence of foregrounds, we present the 2D power spectra of the EoR signal (i.e., without foregrounds or thermal noise) in the 160–170 MHz band for the true values and the MCMC values —the median values of $\zeta = 21.13$, $\log_{10}(T_{\rm vir}) = 4.52$, $L_X/{\rm SFR} = 40.00$, and $E_0 = 0.656$ keV—along with their ratio in Figure 10. The true parameters give a maximum power that is up to six times higher than the MCMC parameters in the EoR window, suggesting that it is deceptively easy to discriminate between the models.

In reality, however, it should be considered that the presence of foregrounds and noise may obscure modes that are vital for differentiation of these models. Figure 11 shows, from left to right: the 2D PS of the data i.e., the EoR signal, thermal noise and point-source foregrounds, and the 2D PS of the true EoR signal along with the difference between these two. The negative power in the right panel is caused by the unaccounted for contribution of the cross-power terms between the EoR signal and the foregrounds and thermal noise. This is because the EoR signal and the expected thermal noise and foregrounds are modeled separately, as mentioned in Section 2.4.

We can estimate cross-power by looking at the variance of the difference between the 2D power spectra of the data (P_D) and the model (P_M) for a single realization of 21 cm power spectrum but with an ensemble of foregrounds and noise realizations following

$$\begin{aligned} {\rm Var}(P_D - P_M) &= {\rm Var}[\langle |(V_{21} + V_{\rm FG} + V_{\rm N})|^2 \rangle_{\boldsymbol{u}} \\ &\quad - \langle |(V_{\rm FG} + V_N)|^2 + |(V_{21})|^2 \rangle_{\boldsymbol{u}}] \\ &= \langle 2P_{21}[{\rm Var}(V_{\rm FG}) + {\rm Var}(V_N)] \rangle^*_{\boldsymbol{u}}, \end{aligned} \quad (23)$$

where V_{21}, $V_{\rm FG}$, and V_N are the visibilities of the EoR signal, foregrounds, and noise respectively. For simplification, $\langle\rangle_{\boldsymbol{u}}$ denotes the cylindrical average in $\boldsymbol{u}$ bin with weighting as described in Section 2.3, and $\langle\rangle^*_{\boldsymbol{u}}$ is the same as $\langle\rangle_{\boldsymbol{u}}$ except that the weighting is squared; see Appendix B for the complete derivation. From the equation, we can see that the variance is largest when P_{21} is larger than the noise and foregrounds. To investigate this further, we present the ratio of the variance of $P_D - P_M$ and the true total variance σ_T^2 in Figure 12. The region that is more correlated than the other modes is at $\boldsymbol{u} \leqslant 30$, whereby the size of the correlated bins are dictated by the correlation lengths of the window functions. This is evident from the red regions in the figure, which extend over 2 $\boldsymbol{u}$ by 4η bins, corresponding to the correlation length of the MWA following D/λ and the Blackman–Harris taper, respectively.

To further explore the region where most of the biasing takes place and gauge the net effect of the cross-power on the

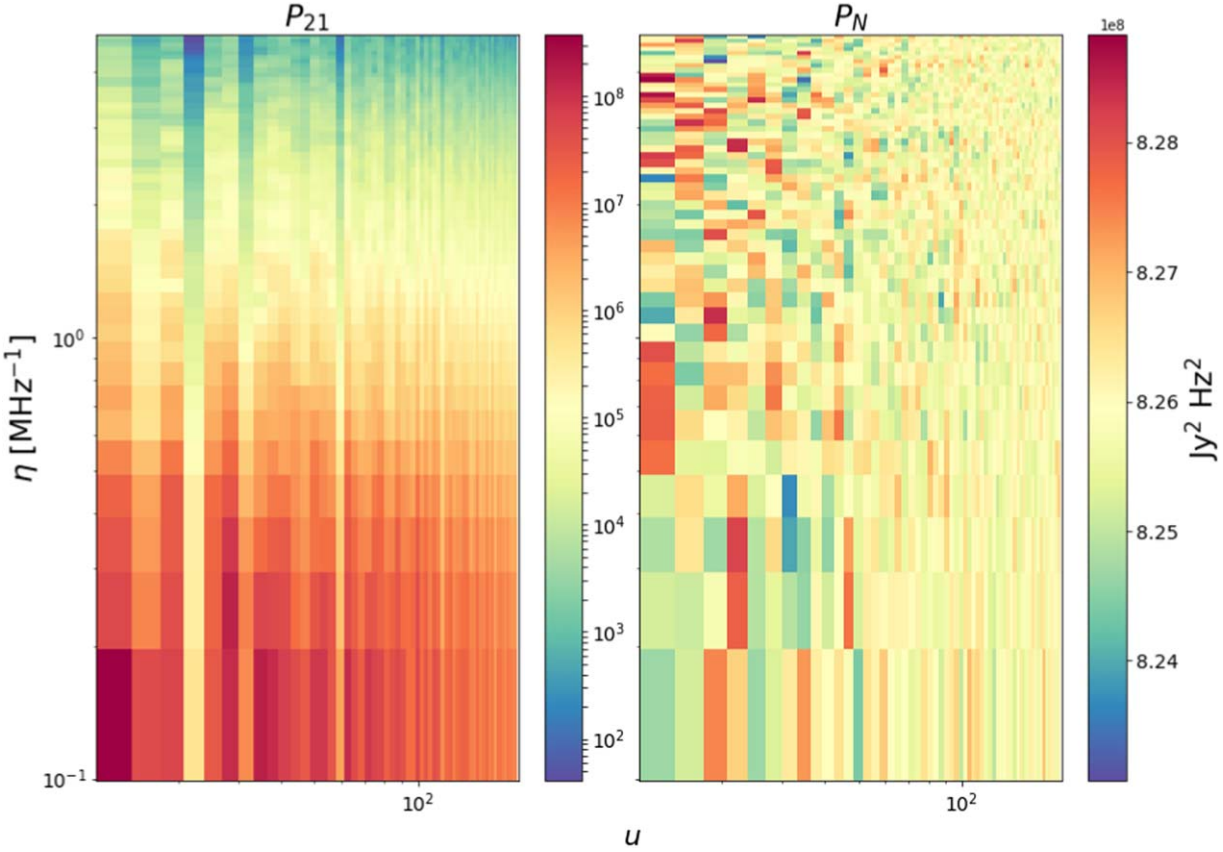

Figure 7. Power spectra of the EoR signal (left) and the thermal noise with the MWA sensitivity (right) in units of Jy^2Hz^2. With the uniform UV sampling, the signal-to-noise ratio is of order unity for 1000 hr of observation time, due to the small collecting area of the MWA. While this is enough for an EoR signal detection over the slope of the 1D PS, it is not sensitive enough for EoR parameter estimation with the MWA.

likelihood, we calculate the pseudo-likelihood ($\hat{\mathcal{L}}$) given by

$$\hat{\mathcal{L}} = -\frac{(P_D - P_M)^2}{\sigma_T^2}. \quad (24)$$

This is a variation of Equation (18) but with σ_T^2 instead of Σ. Figure 13 show—$\hat{\mathcal{L}}$ for the true (left) and MCMC (right) parameters. Here, -$\hat{\mathcal{L}}$ is overall greater for the true parameters, as apparent from the overwhelming red region in the left panel. This region coincides with low $\boldsymbol{u}$, thus supporting our argument that this region is more correlated. With realistic data sets whereby the visibilities from the different components are summed before the PS is calculated, the likelihood has biased signal discrimination power when the same steps are not taken for the model. The likelihood favors whichever EoR model accounts for the cross-power term, thus resulting in biased constraints.

In principle, the signal-to-noise ratio is greater than one in every PS cell outside the wedge, because of our low level of thermal noise. This results in the use of all modes of the PS in calculating the likelihood, including the ones that do not have any real constraining power, i.e., less signal. In addition, because the signal is stronger at modes with $\boldsymbol{u} \leqslant 30$, these modes are more affected by the subtle cross-correlation effects from noise and foregrounds. The deficits in the modeling can thus lead to biased answers, as the likelihood tries to compensate for the missing power.

Because our MCMC runs are shorter and may not have properly converged, the constraints from the MCMC may be invalid. To sample the "true" 1σ contours for a Gaussian posterior, we explore the $\Delta\chi^2$ contours by assuming that the true χ^2 value is identical to the degree of freedom (df) (hence, the 1σ level is $\sqrt{2df}$).

In Figure 14, we present the $\Delta\chi^2$ contours for the three bands using the best-fitting parameters from the MCMC results shown in Figure 9. With $df = 2996$, the 1σ level is $\sim$77. Because the constraints for L_X/SFR and E_0 from the MCMC look reasonably inflated and unbiased, we focus on examining the $\Delta\chi^2$ contours for ζ and $T_{\rm vir}$.

We see that there are multiple regions in the parameter space that satisfy the 1σ condition in the middle and last frequency bands. This can confound the parameter estimation via MCMC. Additionally, we can see that the constraints for $T_{\rm vir}$ are not as tight as shown in Figure 9, but the constraints for the other parameters match the results from the MCMC.

We present the estimated median values of the parameters from each of the MCMC runs in Table 3, with the upper and lower limit being the 1σ level from the $\Delta\chi^2$ grid. In the presence of both foregrounds and thermal noise, $T_{\rm vir}$, L_X/SFR, and E_0 are all within 1σ from the truth for the three frequency bands. For ζ, however, the best-fitting parameter values are off by as much as 5σ due to the unaccounted cross-power terms. This suggests that the effects of ζ on the PS space are primarily at low-$\boldsymbol{u}$ regions, since these modes are significantly impacted by the missing power.

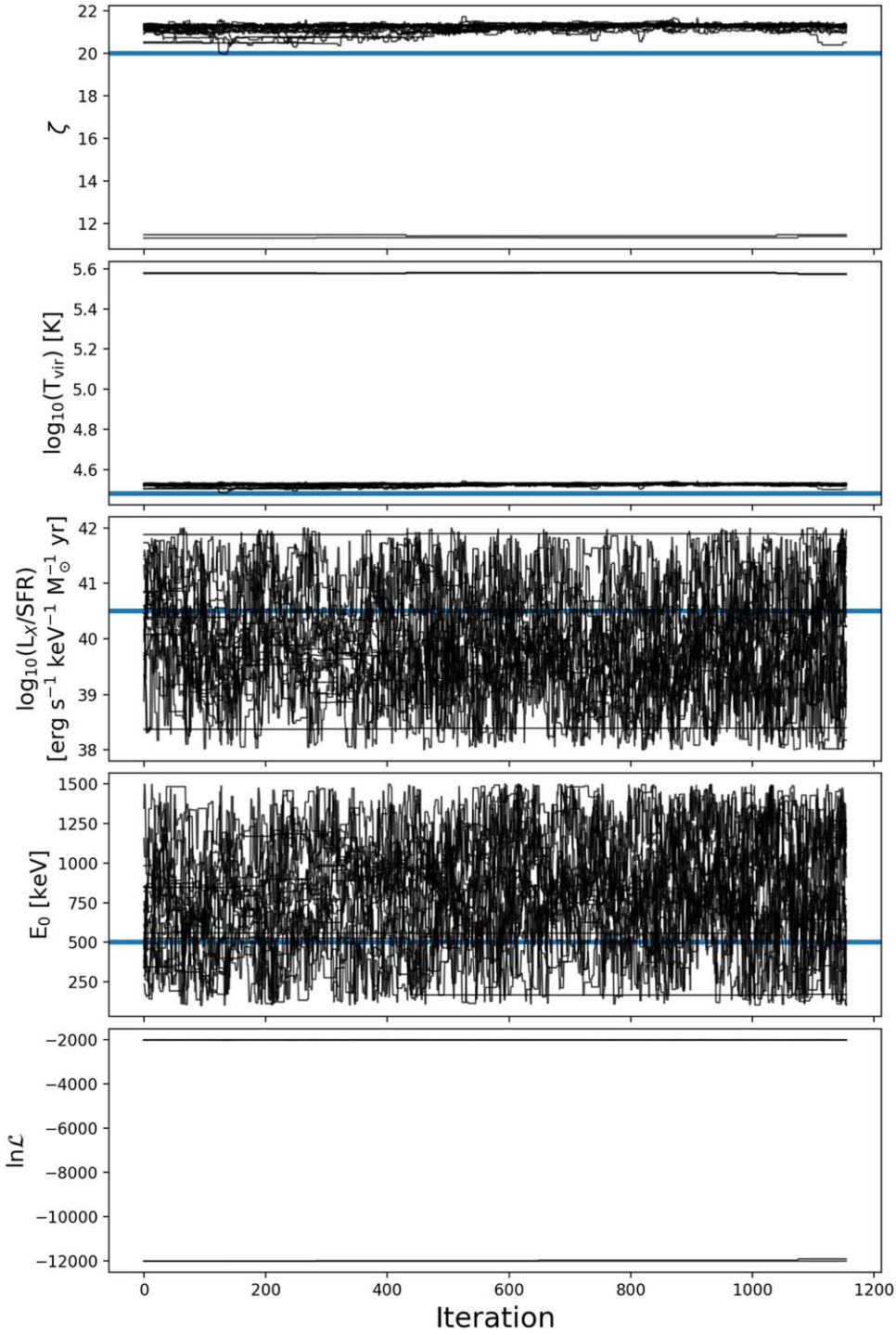

Figure 8. Example trace plot from the 160–170 MHz band with thermal noise and foregrounds. Blue lines show the true value of the parameter, while black lines show the progression of the parameter estimation at each iteration. In this particular case, we have ignored the walkers with $\ln \mathcal{L} < -4000$.

6. Discussion and Conclusion

Our 21CMMC plug-in, PY21CMMC-FG, simulates statistical point-source foregrounds and instrumental components that include a Gaussian beam, UV-sampling, and thermal noise. It uses a Gaussian Fourier beam to regrid the data before spherically averaging it to compute the 2D PS. The 2D PS allows for the use of the entire parameter space in the likelihood computation, effectively ensuring that the effects of foregrounds are accounted for, even in the EoR window.

We show that the implementation of a multivariate normal likelihood and the covariance of the noise and foregrounds appropriately downweight modes that are contaminated by foregrounds, thus optimally accounting for all Gaussian information. Additionally, the low level of noise ensures that all modes in the EoR window are used in calculating the likelihood, even though not all modes actually have constraining power. Due to incomplete sampling of the posteriors and insufficient convergence of the chains, a cross-check with a

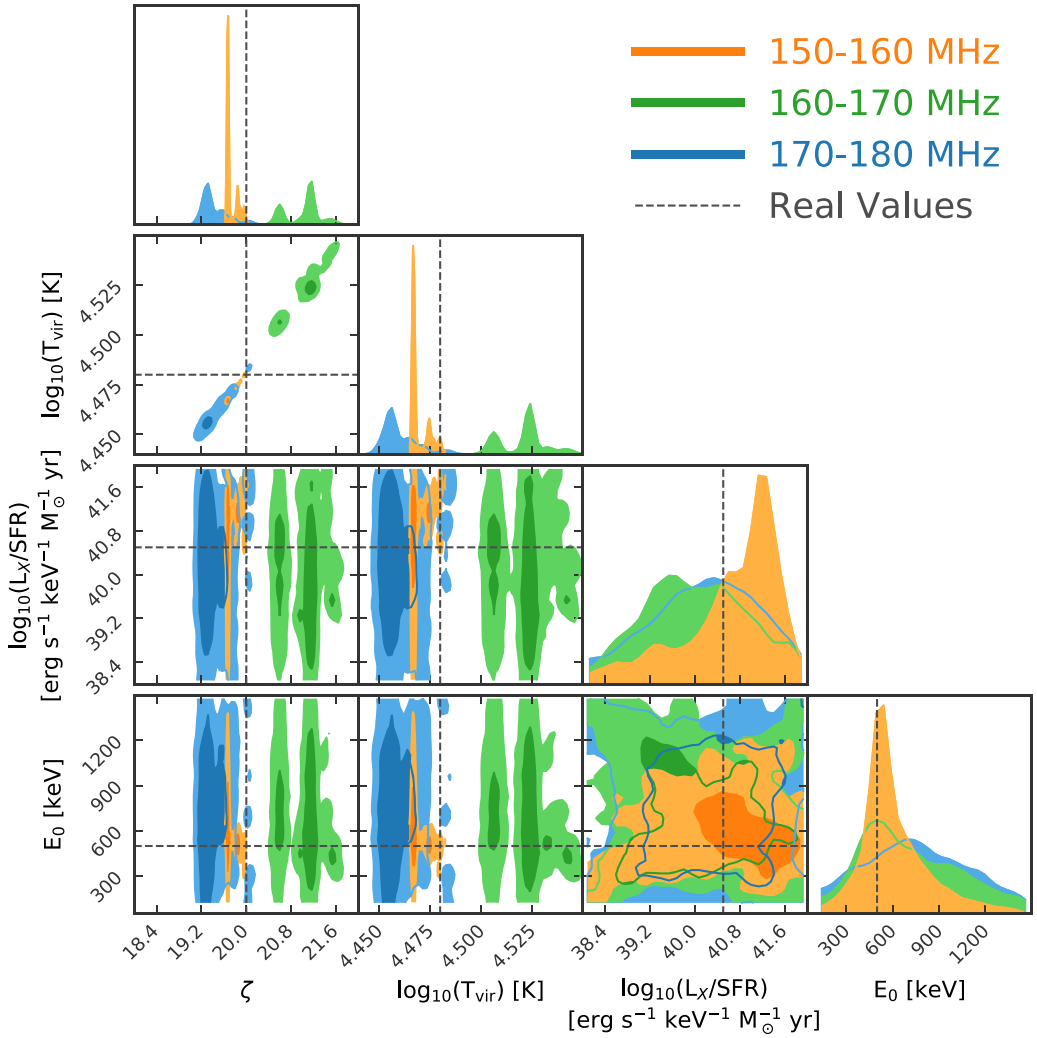

Figure 9. Corner plot comparing the constraints of EoR parameters in the presence of instrumental noise and foregrounds in the different frequency bands: 150–160 (orange), 160–170 (green), and 170–180 (blue) MHz.

Gaussian posterior distribution is needed in order to properly constrain the parameters.

Furthermore, to accurately constrain the parameters, it is imperative that future experiments take into account the cross-power terms between the EoR signal and the foregrounds and noise. This can be done by either properly modeling all the components together, or by quantifying the cross-power terms separately and adding them to the framework we have developed. Nevertheless, both of these approaches may be computationally expensive and require a great deal of memory because the gridded visibilities from all the foregrounds and thermal noise runs need to be stored and added to the EoR signal on each iteration.

Though our research does not address the full complexity of 21 cm parameter estimation experiments, it is the first step toward a more realistic one. In the future, however, it would be useful to include

1. Earth rotation synthesis;
2. The full curved-sky visibility equation, including the *w*-term particularly for the MWA;
3. More realistic, non-Gaussian beams, including nonanalytic ones such as the MWA beam (Sutinjo et al. 2015);
4. Multiredshift parameter estimation;
5. Other systematics such as RFI, ionosphere, gain errors, and cable reflections;
6. Diffuse Galactic foregrounds;
7. Clustered extragalactic point-source foregrounds; and
8. Uncertain foreground parameters.

Out of all these effects, the inclusion of Earth rotation synthesis and Galactic foregrounds are the most important because they can, respectively, lead to a noise level up to 3× higher for longer baselines, as shown by 21CMSENSE, and contain spatially structured signal. Moreover, a further optimization of the code is necessary for more accurate constraints and absolute convergence of the MCMC.

A.N. thanks R.J.J. Poulton and A. Bahramian for their contribution to this research. This work is supported by the Australian Research Council Centre of Excellence for All Sky Astrophysics in 3 Dimensions (ASTRO 3D), through project number CE170100013. C.M.T. is supported by an ARC Future Fellowship through project number FT180100321. The International Centre for Radio Astronomy Research (ICRAR) is a Joint Venture of Curtin University and The University of Western Australia, funded by the Western Australian State government. We acknowledge that the results in this paper

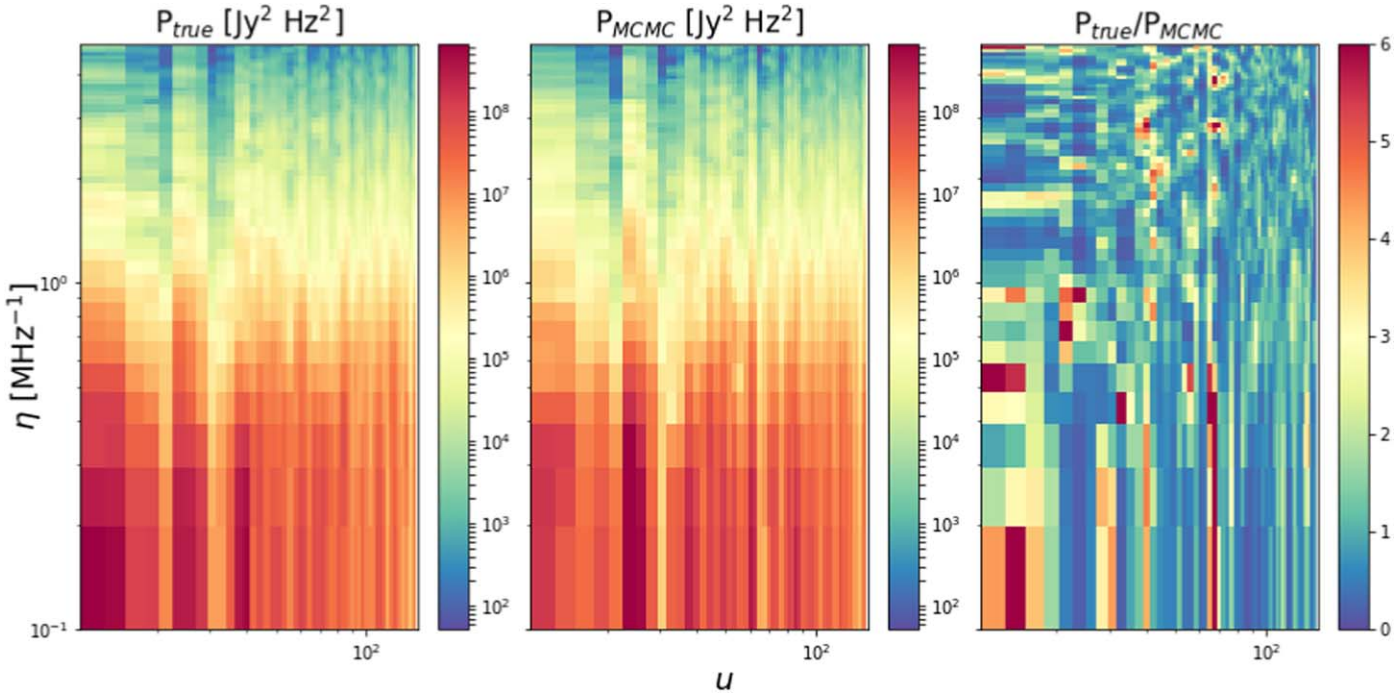

Figure 10. Two-dimensional power spectra of the EoR signal (i.e., without foregrounds or thermal noise) in the 160–170 MHz band for the true values (left) and the MCMC values (middle)—the median values of $\zeta = 21.13$, $\log_{10}(T_{\rm vir}) = 4.52$, $L_X/{\rm SFR} = 40.00$, and $E_0 = 0.656$ keV—along with their ratio. The true parameters give a maximum power that is up to six times higher than the MCMC parameters in the EoR window, suggesting that it is deceptively easy to discriminate between the two models.

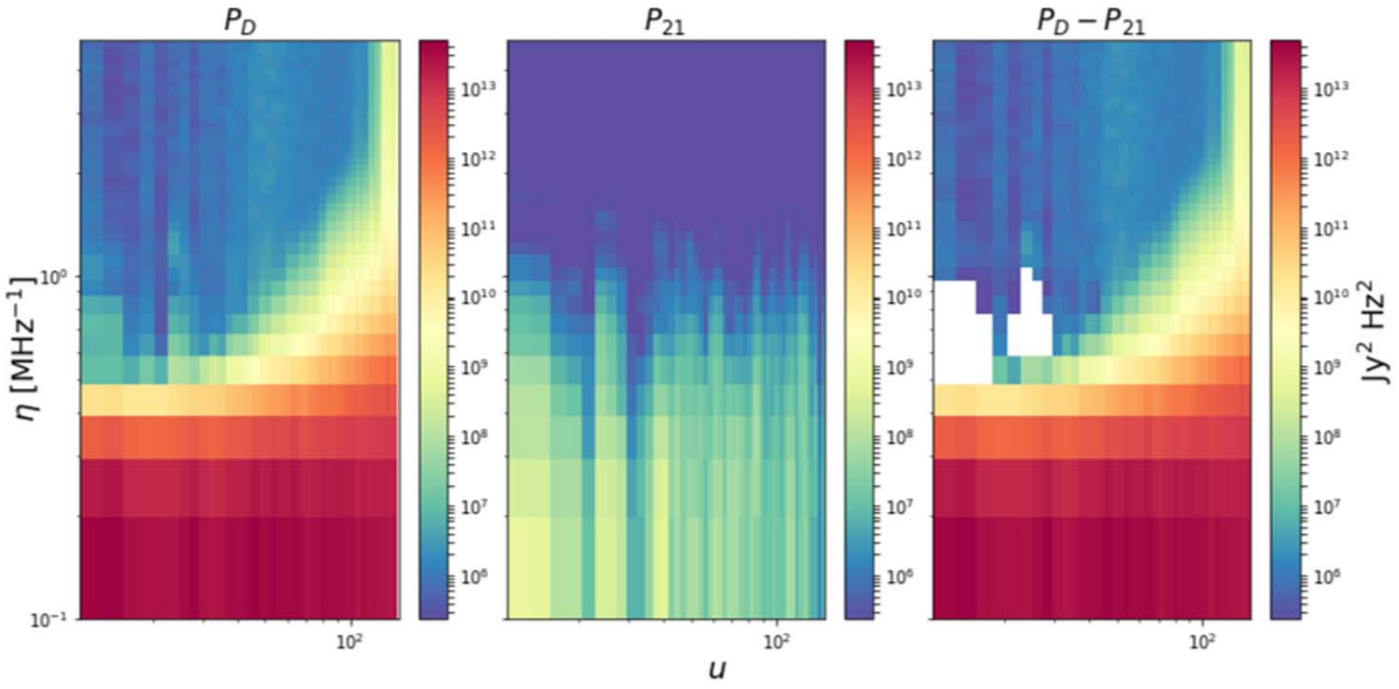

Figure 11. Two-dimensional power spectra of the data, i.e., EoR signal, foregrounds, and thermal noise (left), as well as the EoR signal (middle) in the 160–170 MHz band, along with their difference (right). The negative power (white region) in the right panel is caused by the unaccounted for contribution of the cross-power terms between the EoR signal and the foregrounds and thermal noise.

have been achieved by using resources provided by the Pawsey Supercomputing Centre, with funding from the Australian Government and the Government of Western Australia, as well as OzSTAR, funded by Swinburne University and the Australian Government's Education Investment Fund.

Appendix A
Fourier Conventions

The Fourier transform (hereafter FT) conventions used in this paper are as follows. The continuous n-dimensional FT,

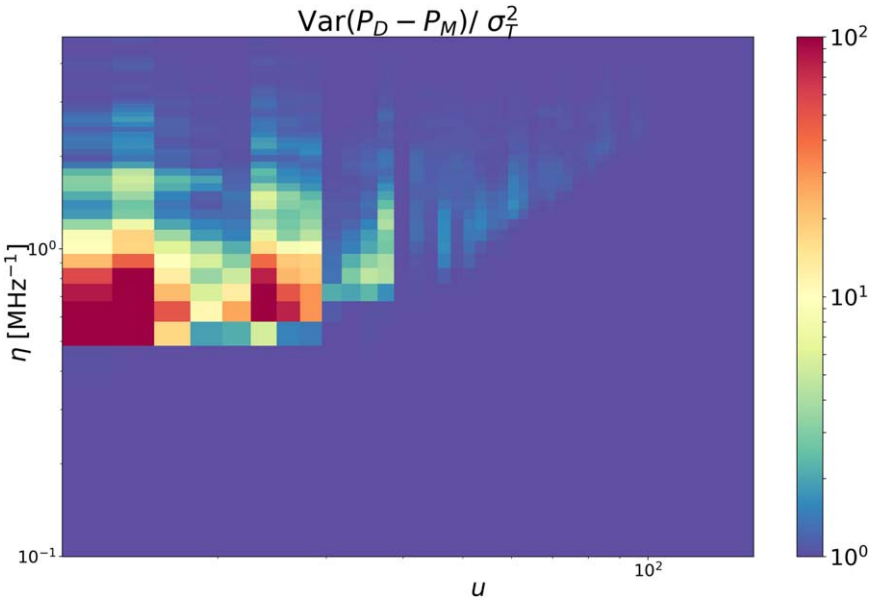

Figure 12. Ratio of the variance of the $P_D - P_M$ to the actual total variance, σ_T.

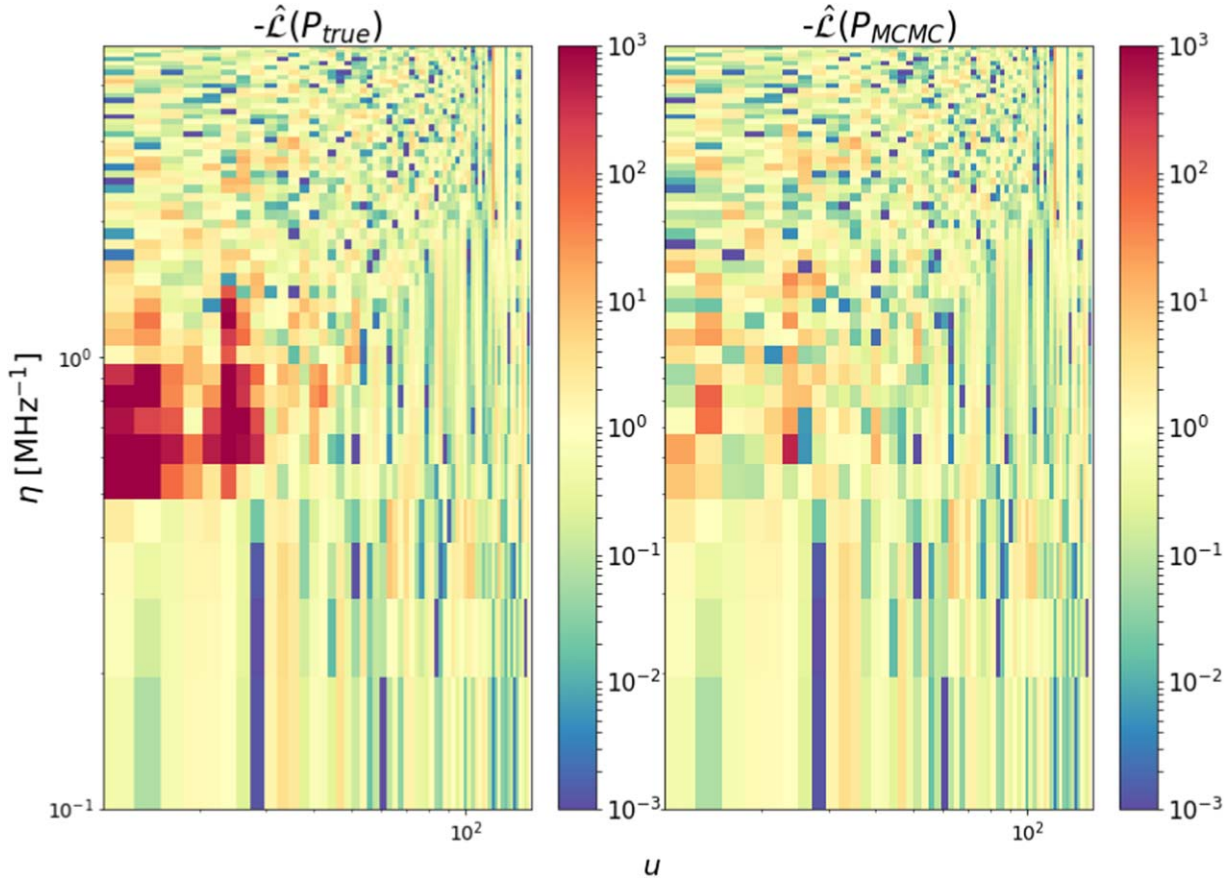

Figure 13. Visualization of $-\hat{\mathcal{L}}$ for the true (left) and MCMC (right) parameters. Overall, $-\hat{\mathcal{L}}$ is greater for the true parameters, as apparent from the overwhelming red region in the left panel coinciding with low u.

$F(\boldsymbol{k})_\infty$, can be written as

$$F(\boldsymbol{k})_\infty = \sqrt[n]{\frac{|b|}{(2\pi)^{1-a}}} \int f(\boldsymbol{r}) \exp(-ib\boldsymbol{k}\cdot\boldsymbol{r}) d^n\boldsymbol{r}, \qquad \text{(A1)}$$

where $\boldsymbol{r}$ is the comoving coordinate in real space, $\boldsymbol{k}$ is the Fourier dual of $\boldsymbol{r}$, and a and b are arbitrary constants (Murray 2018). Conventionally, radio interferometry uses $(a, b) = (0, 2\pi)$, while cosmology uses $(a, b) = (1,1)$. To approximate a continuous FT, a discrete FT normalizes by the physical length of the data set (L) per number of data available

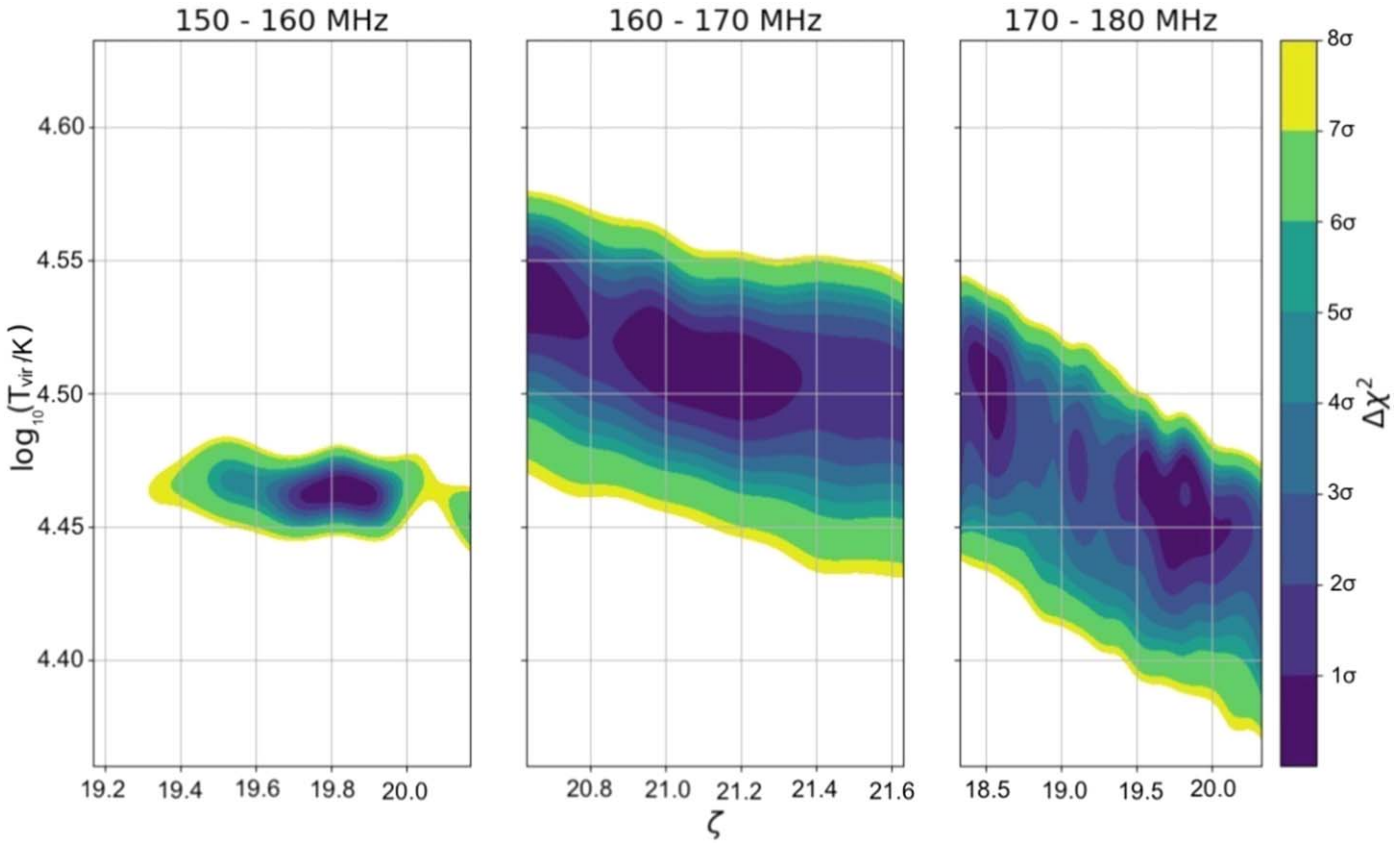

Figure 14. The $\Delta\chi^2$ contours for the three bands using the best-fitting parameters from our framework, which are presented in Table 3. With $df = 2996$, the 1σ level is ~77. Because the constraints for L_X/SFR and E_0 from the MCMC look reasonably inflated, we only focus on examining the $\Delta\chi^2$ contours for ζ and $T_{\rm vir}$.

Table 3
Median Values from the MCMC with 1σ Level from the $\Delta\chi^2$ Grid

		150–160 MHz	160–170 MHz	170–180 MHz
ζ	20	$19.67^{+0.23}_{-0.00}$	$21.13^{+0.18}_{-0.23}$	$19.33^{+0.77}_{-0.00}$
$\log_{10}(T_{\rm vir})$	4.48	$4.47^{+0.01}_{-0.00}$	$4.52^{+0.01}_{-0.04}$	$4.46^{+0.04}_{-0.03}$
$\log_{10}(L_X/\ {\rm SFR})$	40.5	$40.09^{+0.48}_{-1.19}$	$40.00^{+0.99}_{-0.92}$	$40.22^{+0.94}_{-1.06}$
E_0	500	$531.51^{+209.64}_{-34.39}$	$656.50^{+409.39}_{-242.44}$	$739.60^{+385.11}_{-348.29}$

for each dimension (N). The resulting modes, k, measured from the transform are

$$k = \frac{2\pi}{b}\frac{m}{L},\ m \in (-N/2,\ldots,N/2). \tag{A2}$$

Appendix B
Variance of Residual

Let w_i be the weights used in averaging from 3D (u, v, η)-space down to 2D (u, η)-space, and $N^u_{\rm uv}$ is the number of UV cells in a given $|u|$ bin; the variance of P_D is thus

$$\begin{aligned}{\rm Var}({\rm P_D}) &= \frac{\sum_{i\in uv}^{N^u_{uv}} w_i^2 {\rm Var}(\mathcal{Q})}{\left(\sum_{i\in uv}^{N^u_{uv}} w_i\right)^2}\\ &\equiv \langle {\rm Var}(\mathcal{Q})\rangle^*_{\boldsymbol{u}},\end{aligned}$$

where

$$\begin{aligned}\mathcal{Q} = {} & V_{21}V_{21}^\dagger + V_{\rm FG}V_{\rm FG}^\dagger + V_N V_N^{i\dagger}\\ & + 2\mathcal{R}e(V_{21}V_{\rm FG}^\dagger + V_{21}V_N^\dagger + V_{\rm FG}V_N^\dagger).\end{aligned} \tag{B1}$$

In our case, while both $V_{\rm FG}$ and V_N are complex random variables, V_{21} is *not*. We use the same random seed to create the signal that comprises the mock data and all the model realizations throughout the MCMC (though these have different input astrophysics). Essentially, we treat the signal field as deterministic, given the input parameters, and thus ignore cosmic variance. When taking the variance of $\mathcal{Q}$, this leads all cross-terms involving ${\rm Var}(V_{21})$ or ${\rm Var}(P_{21})$ to be zero, leaving

$$\begin{aligned}{\rm Var}(\mathcal{Q}) = {} & {\rm Var}[P_{\rm FG}] + {\rm Var}[P_N] + 4{\rm Var}[\mathcal{R}e(V_{21}V_{\rm FG}^\dagger)]\\ & + 4{\rm Var}[\mathcal{R}e(V_{21}V_N^\dagger)] + 4{\rm Var}[\mathcal{R}e(V_N V_{\rm FG}^\dagger)]\\ & + 4{\rm Cov}[V_{\rm FG}V_{\rm FG}^\dagger, \mathcal{R}e(V_{21}^\dagger V_{\rm FG})] + 4{\rm Cov}[V_N V_N^\dagger, \mathcal{R}e(V_{21}^\dagger V_{\rm FG})]\\ & + 4{\rm Cov}[V_N V_N^\dagger, \mathcal{R}e(V_{21}^\dagger V_N)] + 4{\rm Cov}[V_N V_N^\dagger, \mathcal{R}e(V_N^\dagger V_{\rm FG})]\\ & + 8{\rm Cov}[\mathcal{R}e(V_{21}V_N^\dagger), \mathcal{R}e(V_{\rm FG}^\dagger V_N)],\end{aligned} \tag{B2}$$

and the difference between the data and model variance is

$$\begin{aligned}\Delta{\rm Var}(\mathcal{Q}) = {} & 4{\rm Var}[\mathcal{R}e(V_{21}V_{\rm FG}^\dagger)] + 4{\rm Var}[\mathcal{R}e(V_{21}V_N^\dagger)]\\ & + 4{\rm Cov}[V_{\rm FG}V_{\rm FG}^\dagger, \mathcal{R}e(V_{21}^\dagger V_{\rm FG})] + 4{\rm Cov}[V_N V_N^\dagger, \mathcal{R}e(V_{21}^\dagger V_{\rm FG})]\\ & + 4{\rm Cov}[V_N V_N^\dagger, \mathcal{R}e(V_{21}^\dagger V_N)]\\ & + 8{\rm Cov}[\mathcal{R}e(V_{21}V_N^\dagger), \mathcal{R}e(V_{\rm FG}^\dagger V_N)].\end{aligned} \tag{B3}$$

Assuming both $V_{\rm FG}$ and V_N to be proper complex random variables with a uniform phase distribution, we can simplify to

$$\begin{aligned}\Delta{\rm Var}(\mathcal{Q}) &= 4P_{21}{\rm Var}(V_{\rm FG}^{\mathcal{R}}) + 4P_{21}{\rm Var}(V_N^{\mathcal{R}})\\ &+ 4(V_{21}^{\mathcal{R}} + V_{21}^{\mathcal{I}})[\langle V_{\rm FG}^{3,\mathcal{R}}\rangle - \langle V_{\rm FG}^{2,\mathcal{R}}\rangle\langle V_{\rm FG}^{\mathcal{R}}\rangle]\\ &+ 4(V_{21}^{\mathcal{R}} + V_{21}^{\mathcal{I}})[\langle V_N^{3,\mathcal{R}}\rangle - \langle V_N^{2,\mathcal{R}}\rangle\langle V_N^{\mathcal{R}}\rangle]\\ &+ 8(V_{21}^{\mathcal{R}} + V_{21}^{\mathcal{I}})\langle V_{\rm FG}^{\mathcal{R}}\rangle{\rm Var}(V_N^{\mathcal{R}}),\end{aligned} \tag{B4}$$

where a superscript $\mathcal{R}$ indicates taking just the real component (which is statistically equivalent to the imaginary component). Here, the three-point term in the noise disappears because it is symmetric about zero. Without explicitly modeling the three-point term of the foregrounds, we also assume that it is very much subdominant—there is nothing to favor a negative over a positive foreground visibility component. Recognizing that ${\rm Var}(V^{\mathcal{R}}) = {\rm Var}(V)/2$, we finally obtain

$$\Delta{\rm Var}(\mathcal{Q}) = 2P_{21}[{\rm Var}(V_{\rm FG}) + {\rm Var}(V_N)]. \tag{B5}$$

ORCID iDs

A. Nasirudin https://orcid.org/0000-0003-2213-4547
S. G. Murray https://orcid.org/0000-0003-3059-3823
C. M. Trott https://orcid.org/0000-0001-6324-1766
R. C. Joseph https://orcid.org/0000-0003-3457-4670
C. Power https://orcid.org/0000-0002-4003-0904

References

Barkana, R. 2009, MNRAS, 397, 1454
Barkana, R., & Loeb, A. 2001, PhR, 349, 125
Barkana, R., & Loeb, A. 2005, ApJL, 624, L65
Behroozi, P. S., & Silk, J. 2015, ApJ, 799, 32
Binnie, T., & Pritchard, J. 2019, MNRAS, 487, 1160
Bond, J., Cole, S., Efstathiou, G., & Kaiser, N. 1991, ApJ, 379, 440
Bowman, J. D., Rogers, A. E. E., Monsalve, R. A., Mozdzen, T. J., & Mahesh, N. 2018, Natur, 555, 67
Choudhury, T. R., & Ferrara, A. 2005, MNRAS, 361, 577
Datta, A., Bowman, J. D., & Carilli, C. L. 2010, ApJ, 724, 526
DeBoer, D. R., Parsons, A. R., Aguirre, J. E., et al. 2017, PASP, 129, 045001
Dewdney, P. E., Hall, P. J., Schilizzi, R. T., & Lazio, T. J. L. 2009, IEEEP, 97, 1482
Dodelson, S., & Schneider, M. D. 2013, PhRvD, 88, 063537
Furlanetto, S. R., Oh, S. P., & Briggs, F. H. 2006, PhR, 433, 181
Furlanetto, S. R., Zaldarriaga, M., & Hernquist, L. 2004, ApJ, 613, 1
Gillet, N., Mesinger, A., Greig, B., Liu, A., & Ucci, G. 2019, MNRAS, 484, 282
Gleser, L., Nusser, A., & Benson, A. J. 2008, MNRAS, 391, 383
Greig, B., & Mesinger, A. 2015, MNRAS, 449, 4246
Greig, B., & Mesinger, A. 2017, MNRAS, 472, 2651
Greig, B., & Mesinger, A. 2018, MNRAS, 477, 3217
Harker, G. J., Pritchard, J. R., Burns, J. O., & Bowman, J. D. 2011, MNRAS, 419, 1070
Hassan, S., Davé, R., Finlator, K., & Santos, M. G. 2017, MNRAS, 468, 122
Hogg, D. W. 1999, arXiv:astro-ph/9905116
Intema, H., Van Weeren, R., Röttgering, H., & Lal, D. 2011, A&A, 535, A38
Jacobs, D. C., Hazelton, B., Trott, C., et al. 2016, ApJ, 825, 114
Jelić, V., Zaroubi, S., Labropoulos, P., et al. 2010, MNRAS, 409, 1647
Jordan, C., Murray, S., Trott, C., et al. 2017, MNRAS, 471, 3974
Kern, N. S., Liu, A., Parsons, A. R., Mesinger, A., & Greig, B. 2017, ApJ, 848, 23
Knevitt, G., Wynn, G. A., Power, C., & Bolton, J. 2014, MNRAS, 445, 2034
Liu, A., & Shaw, J. R. 2019, arXiv:1907.08211
Madau, P., Rees, M. J., Volonteri, M., Haardt, F., & Oh, S. P. 2004, ApJ, 604, 484
Mellema, G., Koopmans, L. V. E., Abdalla, F. A., et al. 2013, ExA, 36, 235
Mesinger, A., Ewall-Wice, A., & Hewitt, J. 2014, MNRAS, 439, 3262
Mesinger, A., Furlanetto, S., & Cen, R. 2011, MNRAS, 411, 955
Mevius, M., van der Tol, S., Pandey, V. N., et al. 2016, RaSc, 51, 927
Morales, M. F., Hazelton, B., Sullivan, I., & Beardsley, A. 2012, ApJ, 752, 137
Morales, M. F., & Wyithe, J. S. B. 2010, ARA&A, 48, 127
Murray, S. G. 2018, powerbox: Arbitrarily structured, arbitrary-dimension boxes and log-normal mocks, Astrophysics Source Code Library, ascl:1805.001
Murray, S. G., Trott, C. M., & Jordan, C. H. 2017, ApJ, 845, 7
Ocvirk, P., Gillet, N., Shapiro, P. R., et al. 2016, MNRAS, 463, 1462
Offringa, A., Wayth, R., Hurley-Walker, N., et al. 2015, PASA, 32, e008
Park, J., Mesinger, A., Greig, B., & Gillet, N. 2019, MNRAS, 484, 933
Parsons, A., Pober, J., McQuinn, M., Jacobs, D., & Aguirre, J. 2012, ApJ, 753, 81
Patil, A. H., Zaroubi, S., Chapman, E., et al. 2014, MNRAS, 443, 1113
Planck, P. 2016, A&A, 594, A13
Pober, J. C., Liu, A., Dillon, J. S., et al. 2014, ApJ, 782, 66
Pober, J. C., Parsons, A. R., DeBoer, D. R., et al. 2013, AJ, 145, 65
Pritchard, J. R., & Loeb, A. 2012, RPPh, 75, 086901
Ricotti, M., & Ostriker, J. P. 2004, MNRAS, 352, 547
Schmit, C. J., & Pritchard, J. R. 2017, in IAU Symp. 333, Peering towards Cosmic Dawn (Cambridge: Cambridge Univ. Press), 43
Shimabukuro, H., Yoshiura, S., Takahashi, K., Yokoyama, S., & Ichiki, K. 2017, MNRAS, 468, 1542
Sims, P. H., & Pober, J. C. 2019, MNRAS, 488, 2904
Sobacchi, E., & Mesinger, A. 2014, MNRAS, 440, 1662
Sutinjo, A., O'Sullivan, J., Lenc, E., et al. 2015, RaSc, 50, 52
Taylor, A., & Joachimi, B. 2014, MNRAS, 442, 2728
Thyagarajan, N., Jacobs, D. C., Bowman, J. D., et al. 2015a, ApJL, 807, L28
Thyagarajan, N., Jacobs, D. C., Bowman, J. D., et al. 2015b, ApJ, 804, 14
Tingay, S., Goeke, R., Bowman, J. D., et al. 2013, PASA, 30, e007
Trott, C. M., Jordan, C. H., Murray, S. G., et al. 2018, ApJ, 867, 15
Trott, C. M., Wayth, R. B., & Tingay, S. J. 2012, ApJ, 757, 101
Van Haarlem, M., Wise, M., Gunst, A., et al. 2013, A&A, 556, A2
Vedantham, H., Udaya Shankar, N., & Subrahmanyan, R. 2012, ApJ, 745, 176
Wayth, R. B., Tingay, S. J., Trott, C. M., et al. 2018, PASA, 35, e033